



**HAL**  
open science

## Identification of microscale fracture models for mortar with in-situ tests

Aliaksandra Tsitova, Fabien Bernachy-Barbe, Benoît Bary, Christophe Bourcier, François Hild

► **To cite this version:**

Aliaksandra Tsitova, Fabien Bernachy-Barbe, Benoît Bary, Christophe Bourcier, François Hild. Identification of microscale fracture models for mortar with in-situ tests. *International Journal of Mechanical Sciences*, 2023, 242, pp.107988. 10.1016/j.ijmecsci.2022.107988 . hal-03881223

**HAL Id: hal-03881223**

**<https://hal.science/hal-03881223v1>**

Submitted on 1 Dec 2022

**HAL** is a multi-disciplinary open access archive for the deposit and dissemination of scientific research documents, whether they are published or not. The documents may come from teaching and research institutions in France or abroad, or from public or private research centers.

L'archive ouverte pluridisciplinaire **HAL**, est destinée au dépôt et à la diffusion de documents scientifiques de niveau recherche, publiés ou non, émanant des établissements d'enseignement et de recherche français ou étrangers, des laboratoires publics ou privés.

## Highlights

### **Identification of microscale fracture models for mortar with in-situ tests**

Aliaksandra Tsitova, Fabien Bernachy-Barbe, Benoît Bary, Christophe Bourcier, François Hild

- *In situ* flexural tests on notched mortar beams monitored via X-ray tomography
- Damage simulations on microstructure-based mesh with DVC measured boundary conditions
- Forces and fracture paths well reproduced using phase-field model
- Adding cohesive elements at matrix-aggregate interfaces altered predicted crack path
- This study shows the potential of microscale simulations for model identification and validation at the microscale

# Identification of microscale fracture models for mortar with in-situ tests

Aliaksandra Tsitova<sup>a,b</sup>, Fabien Bernachy-Barbe<sup>c</sup>, Benoît Bary<sup>a</sup>, Christophe Bourcier<sup>a</sup>, François Hild<sup>b</sup>

<sup>a</sup>Université Paris-Saclay, CEA, Service d'Étude du Comportement des Radionucléides, Gif-sur-Yvette, 91191, France

<sup>b</sup>Université Paris-Saclay, CentraleSupélec, ENS Paris-Saclay, CNRS, LMPS – Laboratoire de Mécanique Paris-Saclay, 91190, Gif-sur-Yvette, France

<sup>c</sup>CEA, DES, IRESNE, DEC, Cadarache, 13108, Saint-Paul-lez-Durance, France

---

## Abstract

The microscale fracture modeling of concrete requires explicit descriptions of the microstructure and the fracture properties of its constituents. The identification of fracture properties of mortar was carried out by numerical analyses of two *in situ* (via X-ray tomography) mesoflexural tests on small-scale specimens. A realistic mesh was created for mechanical simulations to be run. The experimental kinematic fields were measured by processing the reconstructed volumes via Digital Volume Correlation. The measured displacements were used as kinematic boundary conditions to simulate three-point flexural tests. The full dataset consisting of realistic geometry and experimental boundary conditions, allowed for full simulations of the performed tests. A phase-field model for brittle materials was selected to describe damage of the cement paste, and debonding at the matrix-aggregate interfaces was modeled with a cohesive zone model. The fracture paths and ultimate forces simulated with the phase-field model were consistent with the experiment thanks to representative microstructure and boundary conditions. In both tests, the predicted crack path changed because of interface debonding. The introduction of cohesive interface elements did not significantly improve the faithfulness of the path prediction. This study demonstrates the potential of microscale simulations of *in situ* tests for model identification, validation and development at the microscale of mortar.

**Keywords:** Cohesive zone model, damage, digital volume correlation, microscale, phase-field model, X-ray tomography

---

## 1. Introduction

Fracture in civil engineering structures is a problem of primary importance, and damage prediction approaches are being developed at both structural [1; 2; 3] and lower scales [4; 5; 6]. Cementitious materials have a complex heterogeneous microstructure at meso- and microscales. As a consequence, the fracture process depends on the granular assembly and its size, shape and spatial distributions, as well as on the fracture properties of constituents. Cracking in heterogeneous materials is a complex phenomenon consisting of microcrack initiation at Interfacial Transition Zones (ITZs) and in the bulk cement paste, subsequent propagation, with potential branching and coalescence of macrocracks. Homogeneous damage models may not always predict the exact crack path as they do not account for material heterogeneity and corresponding differences of mechanical properties of individual phases. Microscale modeling has become a promising method for the simulation of complex damage patterns and for gaining a better understanding of fracture processes at lower scales as it allows the influence of different phases such as cementitious matrix, aggregates, ITZs and voids to be investigated [7; 8; 9]. Besides mechanical aspects, mesoscale models may be coupled with viscous, diffusive and thermal models, which may also assign different behavior to specific phases [9; 10].

Initially, two groups of methods were used to model microstructures. In direct methods, the generated aggregates of different shapes and sizes were randomly packed into a closed volume and embedded within cementitious or mortar matrices to form digital specimens [11; 12; 13; 14; 15; 16; 17]. In indirect methods, the different phases are not explicitly modeled. Instead, heterogeneous material properties are simulated as spatially-varying random fields assigned to FE meshes [18; 19; 20; 21]. However, these techniques lack realistic aggregate morphologies. The introduction of imaging via X-ray Computed Tomography (XCT) in material sciences made it possible to obtain accurate and detailed microstructure characterization that could be used as input for microscale finite element models [22]. The random spatial distribution techniques could also be combined with real aggregate morphology obtained by XCT [23]. In recent years, studies on fracture in concrete with realistic aggregate distributions were carried out using lattice models [24; 25], cohesive elements [26; 27], damage/plasticity models [28], phase field models (PFMs) [29; 30], material point methods (MPMs) [6] and localizing gradient damage models (LGDM) [31]. In addition to heteroge-

36 neous cementitious materials, image-based modeling was performed to study  
37 the failure of the pure cement paste [32].

38 Beyond static imaging of microstructures, XCT was used to monitor initia-  
39 tion and growth of damage via *in situ* tests [33; 34; 35]. Simulations of *in situ*  
40 tests performed in X-ray scanners allowed models to be calibrated and validated  
41 not only by fitting them to macroscopic force-deflection curves, but also by di-  
42 rect comparisons of simulated fracture patterns with experimental observations  
43 [36; 37]. It was concluded that among several sets of parameters leading to simi-  
44 lar force-deflection responses, the most reliable was the one that most accurately  
45 reproduced real fracture. When microscale modeling was considered, attention  
46 was given to the influence of ITZs on crack patterns and material strength; di-  
47 rect simulations were carried out to study the effect of mortar-aggregate inter-  
48 faces in three-point flexure [36; 37], Brazilian tests [38], uniaxial tension [39; 40],  
49 and uniaxial compression [39; 41]. Another step toward a better representation  
50 of complex fracture patterns, besides the use of image-based meshes, was the in-  
51 troduction of experimental Boundary Conditions (BCs). Kinematic BCs measured  
52 via Digital Image Correlation (DIC) or Digital Volume Correlation (DVC) [42; 43]  
53 allow realistic mixed-mode fracture patterns to be simulated [44].

54 A PFM was selected herein. The first version of PFMs was formulated for  
55 brittle fracture [45; 46]. Besides the initial formulation, extensions for cohesive  
56 fracture [47; 48; 49; 50; 29], interfacial cohesive fracture [51], ductile fracture [52],  
57 mixed tensile and compressive shear fracture [53; 54; 55] and interface fracture  
58 in hybrid structures [56] were developed. The need for preexisting cracks and  
59 a priori defined paths were overcome with such models with an energy mi-  
60 nimization approach [57] and the introduction of an auxiliary phase-field va-  
61 riable [58]. The PFM has become an attractive solution for fracture modeling  
62 since it could predict complex crack patterns including initiation, propagation  
63 and coalescence with no need to algorithmically handle these changes in crack  
64 topology [59]. The model was implemented in several ways. Monolithic schemes  
65 were proposed [46], where the mechanical and phase-field equations are fully  
66 coupled and solved simultaneously. Staggered schemes [45], where the two pro-  
67 blems are solved independently and sequentially, were also implemented via ex-  
68 plicit [45; 60; 61], implicit [62; 60] and semi-implicit formulations [63]. The stress  
69 degradation caused by tensile cracking was introduced using spectral decompo-  
70 sition [45] or spherical-deviatoric split [62].

71 Phase-field models are usually associated with high computational costs,  
72 which are due to the extremely fine mesh necessary for crack resolution. Se-  
73 veral modifications have been proposed to alleviate this issue, where the PFM

74 is coupled with mesh refinement algorithms that operate near the vicinity of  
75 cracks, such as adaptive mesh refinement [64; 65], or local refinements with non-  
76 conforming meshes [66]. In more recent developments, PFMs were coupled with  
77 Physics Informed Neural Networks (PINN) [67], which allowed discretization is-  
78 sues to be avoided and computational costs to be significantly reduced.

79       Microscale fracture modeling of mortar calls for explicit descriptions of the  
80 microstructure and the fracture behavior of individual phases. This type of infor-  
81 mation cannot be obtained by means of conventional laboratory destructive tests  
82 that give access to global properties (*e.g.*, strength, fracture energy, elastic mo-  
83 dulus) for heterogeneous materials. For these reasons, in this study, the identifi-  
84 cation of microscopic fracture properties of mortar was carried out by numerical  
85 analyses of *in situ* mesoflexural tests on small-scale (*i.e.*,  $5 \times 5 \times 20$  mm) mor-  
86 tar specimens. The microstructure was characterized on high-quality XCT scans  
87 acquired before each test, thereby resulting in better segmentation quality. The  
88 segmented microstructures were used in the Finite Element (FE) discretization,  
89 which consisted of a microstructure-based mesh in the crack propagation zone  
90 and homogeneous zones for intact parts of the beam. Furthermore, experimen-  
91 tal kinematic fields were measured by processing the reconstructed volumes via  
92 DVC [68]. The measured displacements were used as kinematic BCs to simulate  
93 two three-point flexural tests.

94       Phase-field models for brittle materials led to good predictions of crack mor-  
95 phology in simulations with experimental BCs measured via DIC in 2D macro-  
96 scopic homogeneous analyses [69] and via DVC in 3D mesoscopic computa-  
97 tions [70]. In view of its successful application in these works, the staggered  
98 PFM for brittle fracture with operator split [45] was selected to describe damage  
99 in hydrated cement paste in this study. The description of ITZs as small-thickness  
100 elements may lead to too fine meshes and prohibitive computational costs. Re-  
101 presenting the matrix-aggregate interfaces as zero-thickness cohesive elements  
102 may allow this limitation to be overcome [7; 8; 71]. Interface debonding was si-  
103 mulated with the Cohesive Zone Model (CZM) based on the proposition of [71]  
104 and implemented in the Mfront code generator ([www.tfel.sourceforge.net](http://www.tfel.sourceforge.net)) for  
105 simulations in the FE code Cast3m ([www-cast3m.cea.fr](http://www-cast3m.cea.fr)). One originality of the  
106 present approach lies in using the PFM to represent cracking in the pure cement  
107 paste matrix and combining it with CZM to take into account weaker interfaces  
108 between the cementitious matrix and inclusions.

109       The full dataset, consisting of realistic geometry and experimental BCs, allo-  
110 wed for full simulations of the performed tests and for the calibration of material  
111 parameters for the chosen damage models that may realistically reproduce the

112 observed crack pattern. Figure 1 summarizes the different steps of the present  
 113 study. To the authors' knowledge, such experimental and numerical framework  
 114 allowed, for the first time, the fracture in mortar to be studied at the microscale  
 115 in three dimensions. Carrying out the simulations on the whole sample with  
 116 DVC-based boundary conditions gave more accurate representations of the ex-  
 117 periment, which was crucial for good reproducibility of the results.

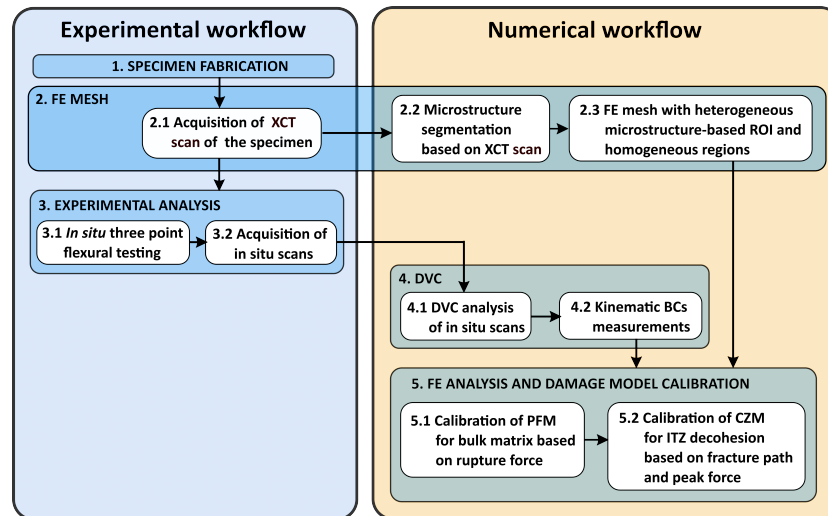


FIGURE 1 – Experimental and numerical workflow implemented herein for the identification and validation of microscopic damage models.

## 118 2. Material and Method

119 In this section, the mortar formulation and sample preparation procedure are  
 120 presented. The experimental protocol of the two *in situ* mesoflexural tests are  
 121 then introduced along with the results. Realistic finite element meshes of mortar  
 122 samples were then constructed. DVC analyses were carried out to measure ki-  
 123 nematic fields, analyze the cracking process and determine boundary conditions  
 124 for the subsequent simulations. Last, detailed descriptions of the phase-field mo-  
 125 del for brittle fracture of hydrated cement paste and the cohesive zone model for  
 126 ITZ debonding are provided.

### 127 2.1. Material and Specimen

128 The mortar formulation is given in Table 1. The batch was mixed using a  
 129 CEM I Portland cement with a water-to-cement ratio of 0.525. A low sand-to-  
 130 binder ratio was used (sand-to-cement = 0.5, sand volume fraction 18%). Sand

131 was sieved to obtain a granulometric distribution within the range 200  $\mu\text{m}$  to  
 132 2 mm in diameter. The reduction of the sand volume fraction and elimination of  
 133 fine particles can be considered as a compromise between making the resulting  
 134 microstructure more suitable for efficient image processing, as less geometric  
 135 details would be distorted or lost, and the representativeness of the obtained  
 136 material relative to real mortar.

TABLE 1 – Mortar constituents.

Constituents	Proportion, kg	Mass density, $\text{kg/m}^3$
Cement CEM I 52.5 N CE CP2 NF Gaurain	320	3,100
Sand 0/4 REC LGP1 (from 200 $\mu\text{m}$ to 2 mm in diameter)	160	2,600
Total water	171.8	1,000

137 A thin mortar plate with dimensions  $65 \times 35 \times 8$  mm was cast in a silicon  
 138 mold and demolded after 1 day. By means of X-ray radiography, the mortar plate  
 139 was checked for the absence of microcracking and defects. After control, the  
 140 plate was selected for further fabrication steps. First, the top surface was ground  
 141 and polished until a 5 mm thickness was reached with simultaneous control of  
 142 parallelism of the top and bottom faces. The thickness deviation was of the order  
 143 0.1 mm, which corresponded to a  $<1.5\%$  inclination between the top and bottom  
 144 surfaces. Second, the plate width was adjusted to 20 mm with a wire saw. Third,  
 145  $5 \times 5 \times 20$  mm beams were cut from the plate with a diamond disk saw to ensure  
 146 planar parallel sides. Fourth, the notch was machined with a saw equipped with a  
 147 fine (0.1 mm) wire and low tension to avoid sample degradation. The notch width  
 148 was approximately 0.15 mm, and its height 1.5 mm. The samples were stored at  
 149 100% air humidity until testing. During preparation, the specimen surfaces were  
 150 rewetted to prevent them from drying induced cracking.

## 151 2.2. *In situ* mesoflexural test

152 The *in situ* flexural tests were performed with the LMPS *in situ*  
 153 Tension - Compression (TC) testing machine designed at MATEIS laboratory [33],  
 154 and an adapted set-up for three-point flexural tests [68]. The load capacity was  
 155  $\pm 1\text{kN}$ . The *in situ* tests consisted of several loading steps, and CT scans were per-  
 156 formed at sustained constant load. Thin adhesive tape was attached to the top  
 157 and bottom faces of the beam for maintaining the sample and improving its sta-  
 158 bility during testing. A schematic representation of CT scans, taken during the  
 159 test, are shown in Figure 2.

160 The *in situ* scans with  $8.8 \mu\text{m} / \text{vx}$  resolution were acquired with the Phoe-  
 161 nix v|tome|x m scanner. First, two successive scans were performed on the un-  
 162 deformed specimen for uncertainty quantification. A small preload of 1 N was  
 163 applied to keep the specimen stable. Then, axial displacements were applied with  
 164  $0.5 \mu\text{m/s}$  rate until sample failure. The experimental configuration along with the  
 165 specimen geometry did not allow for a fine control of crack initiation and its ini-  
 166 tial propagation. Failure was brittle, followed by substantial force drop, and very  
 167 fast crack propagation on the major part of the ligament (Figure 3). It can be  
 168 noted that the crack stability in three-point flexure depends on the sample geo-  
 169 metry and notch depth, as well as the stiffness of the testing setup [72]. Therefore,  
 170 control of fracture propagation may be improved in further studies by modifying  
 171 the beam dimensions. Further, since the aggregate volume fraction in mortar was  
 172 reduced, it may result in a more brittle behavior. The second scan was carried out  
 173 immediately after fracture. After each loading, a 10 min dwell was applied be-  
 174 fore the next scan (*i.e.*, until sufficient decrease of the force relaxation rate). More  
 175 details on the experimental set-up, protocol and XCT acquisition parameters are  
 176 provided in Ref. [68].

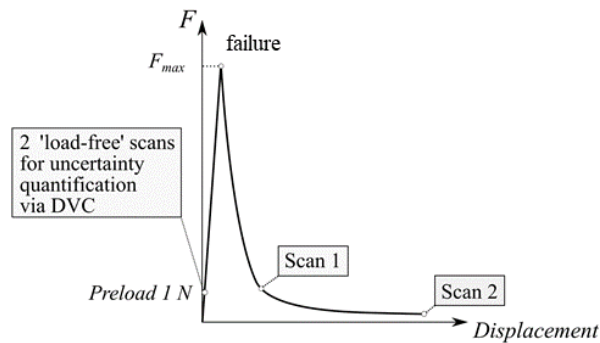


FIGURE 2 – Schematic representation of the force-displacement response of mesoflexural tests with indications when the CT scans were performed.

177 In this study, two *in situ* mesoflexural tests designated as A and B were used  
 178 for model identification purposes. The two tests represent different cases of frac-  
 179 ture propagation due to the loading conditions in combination with the granular  
 180 assembly and its features around the notch root (Figure 3). In test A, the load was  
 181 applied off-axis and several large aggregates were in the plane passing through  
 182 the notch root and loading pin. It resulted in an asymmetric crack with bifurca-  
 183 tion of the fractured surface into two main cracks (Figures 3(a), 5(a), and 12(d,h,l)).

184 In test B, the load was centered and the inclusions in the notch-loading pin plane  
185 were relatively small. The crack did not deviate significantly from a flat path (Fi-  
186 gures 3(b), 5(b), and 13(d,h,l)). In both tests, the fractured surfaces crossed the  
187 cement paste, ITZs and a few limestone aggregates. Cracking of limestone ag-  
188 gregates was observed [73], and was attributed to high fracture toughness of the  
189 limestone-cement matrix interface.

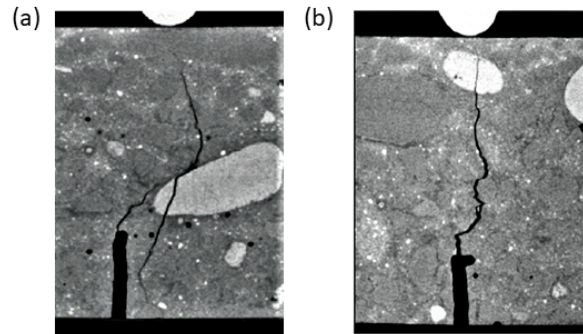


FIGURE 3 – Post-mortem tomographic sections of fractured samples : (a) test A with asymmetric and bifurcated crack (cross-section at  $x = 1.5$  mm depth), and (b) test B with single and essentially vertical fracture ( $x = 1.2$  mm). The height of the samples was 5 mm.

190 The experimental set-up did not allow for a measurement system for meso-  
191 beam deflection and Crack Mouth Opening Displacement (CMOD). For this reason,  
192 apart from DVC measurements, the information about sample deformation before  
193 and at failure onset was not available. After fracture, the residual forces  
194 did not reduce below 5%  $F_{max}$  in all conducted tests. It is likely that the tension  
195 of the adhesive tape applied to the specimens and friction of the aluminum parts  
196 of the bending set-up may have induced additional forces that were of the order  
197 of 5 N (significant at this scale). Therefore, the measured peak force does not  
198 correspond to the failure load. For modeling purposes, the peak force corrected  
199 by the residual force at the end of the test was used as the maximum force.

200 The measured peak forces and estimated flexural strength are reported in  
201 Table 2. The corrected flexural strength of mortar with reduced sand fraction  
202 (sand-to-cement 0.5) was  $8.6 \pm 0.5$  MPa, which is higher than the tensile strength  
203 of standard mortar 6.6 MPa (sand-to-cement 2.127) measured by Brazilian tests  
204 on 30-mm in diameter disks [74].

TABLE 2 – Experimental forces measured in the two mesoflexural tests and corresponding flexural strength.

Test	Measured peak force, N	Residual force, N	Corrected peak force, N	Corrected flexural strength, MPa
A	28.4	7.5	20.9	8.1
B	29.6	1.8	27.8	9.1

205 *2.3. Meshes for finite element simulations*

206 Before the *in situ* test, a high quality scan of the central part of the microbeam  
 207 was acquired with a 5.3  $\mu\text{m}$  / vx resolution using the same CT system. Then, the  
 208 procedures of microstructure segmentation and heterogeneous FE mesh generation,  
 209 which are detailed in [68], were applied to samples A and B. In order  
 210 to model the entire specimen in mechanical simulations, homogeneous regions  
 211 with four-noded tetrahedral elements were added to the microstructure-based  
 212 mesh, denoted as Region Of Interest (ROI), with the open-source python library  
 213 Combs [75] based on the tools of Salome<sup>®</sup> platform (Figure 4).

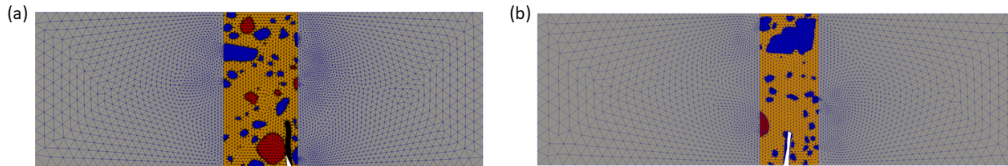


FIGURE 4 – Side view of three-dimensional FE meshes for fracture simulations. (a) Mesh A (corresponding to the microstructure shown in Figure 3(a)), (b) mesh B (corresponding to the microstructure shown in Figure 3(b)). Gray : homogeneous undamaged zone, orange : cementitious matrix, blue : siliceous aggregates, red : limestone aggregates.

214 The element size gradation (*i.e.*, maximum ratio between the lengths of two  
 215 adjacent edges) in the homogeneous regions was set to 1.05. The mesh charac-  
 216 teristics are listed in Table 3. The equivalent element size is defined as the cube  
 217 root of the volume element, and  $h_{el}$  denotes the average size of the elements in  
 218 the mesh.

TABLE 3 – FE mesh characteristics.

	Mesh A	Mesh B
ROI dimensions (width $\times$ height $\times$ length), mm	$4.7 \times 4.73 \times 2.3$	$4.5 \times 4.8 \times 1.8$
ROI mean element size $h_{el}$ , $\mu\text{m}$	32	32
Number of elements in ROI	$1.5 \times 10^6$	$1.19 \times 10^6$
Full mesh dimensions (width $\times$ height $\times$ length), mm	$4.7 \times 4.73 \times 13.95$	$4.51 \times 4.84 \times 15.31$
Total number of elements	$1.9 \times 10^6$	$1.5 \times 10^6$

#### 219 2.4. DVC-based boundary conditions

220 DVC measures the displacement field  $\mathbf{u}$  in selected ROIs by registering the  
 221 deformed volume  $g$  and the reference volume  $f$  assuming gray level conserva-  
 222 tion [42]. In finite element based DVC (FE-DVC), the sought degrees of freedom  
 223 (DOFs) are the nodal displacements of a finite element discretization, and the  
 224 trial fields are the corresponding shape functions [76]. The gray level residual  
 225 field  $\rho(\mathbf{x}) = f(\mathbf{x}) - g(\mathbf{x} + \mathbf{u}(\mathbf{x}))$  represents the difference between the volume  
 226 in the reference configuration and in the deformed state corrected by the measur-  
 227 ed displacement field  $\mathbf{u}$ . The DVC solution is based on the minimization of the  
 228 global residual  $\Phi_c$ , which is equal to the root mean square (RMS) of the residual  
 229 field  $\rho$ . Therefor,  $\Phi_c$  serves as an indicator of the consistency of the solution, nam-  
 230 ely, a smaller global residual means a more trustworthy solution. Local high  
 231 absolute residuals may mark, for example, the presence of discontinuities in dis-  
 232 placements, which in particular cases correspond to cracks [77; 78; 79].

233 The initially formulated correlation problem may become ill-posed for very  
 234 fine meshes, and may require the introduction of a penalty term to make it well-  
 235 posed. In regularized DVC, the linear elastic behavior is enforced locally by the  
 236 introduction of a mechanical penalty  $\Phi_m$  term based on the equilibrium gap [80;  
 237 81; 82]. The global minimization is then performed on the weighted sum of the  
 238 normalized cost functions  $\tilde{\Phi}_c^2 + w_m \tilde{\Phi}_m^2$  (for more details, see [68]). The weight  
 239  $w_m$  is proportional to a regularization length raised to the fourth power  $\ell_{reg}^4$ . If  
 240 the chosen  $\ell_{reg}$  is greater than the element size, the mechanically inadmissible  
 241 displacement fluctuations, which may correspond to cracks or localized plastic  
 242 strains, are smeared over a spatial domain whose size depends on  $\ell_{reg}$  [82; 79].  
 243 DVC calculations were performed within the Correli 3.0 framework developed  
 244 at LMPS [83].

245 The *in situ* scans were binned to lower the computational costs. The resulting  
 246 physical voxel size was  $17.6 \mu\text{m}/\text{vx}$ . The mechanical regularization was based

247 upon homogeneous, isotropic and linear elasticity [80; 82]. The finite element  
248 meshes used for DVC analyses were uniform. They were reconstructed based on  
249 the external surfaces of the samples, obtained by segmentation in Avizo<sup>®</sup>. Surface  
250 meshes were then exported in .stl format and used to generate volumetric meshes  
251 via *Gmsh* (<http://gmsh.info/>) with four-noded tetrahedra. The mean element size  
252 was 7 vx, and the number of elements was in the range  $186 - 199 \times 10^3$ .

253 Uncertainty quantifications were carried out by performing DVC analyses on  
254 the two scans acquired on undeformed specimens. A relaxation procedure was  
255 performed for both tests starting with a regularization length of  $\ell_{reg} = 120$  vx  
256 down to 30 vx. During relaxation, the displacement field obtained after conver-  
257 gence at higher  $\ell_{reg}$  was used then to initialize the next step with lower regula-  
258 rization weight. Such step-by-step process allowed most of the uncertainties to  
259 be filtered out in the first steps and then iteratively converge to a good solution.  
260 The baseline RMS residuals of tests A and B at  $\ell_{reg} = 30$  vx were close (*i.e.*, 1, 360  
261 and 1, 420 gray levels, respectively). The displacement uncertainty was several  
262 times higher for case B (*i.e.*, 2.2  $\mu\text{m}$ ) than for test A (0.6  $\mu\text{m}$ ).

263 Then, the DVC procedure was run between the undeformed and post-mortem  
264 scans. The relaxation procedure was performed again for both tests starting with  
265 a regularization length of  $\ell_{reg} = 120$  vx down to 30 vx. Regularization lengths  
266 less than 30 vx did not bring significant changes in displacements at the contact  
267 zones between the samples and the flexural set-up where BCs were measured.  
268 The residual fields are shown in Figure 5. The highest absolute levels correspond  
269 to the fractured surfaces. Well defined residuals around cracks and the absence of  
270 high levels in intact areas demonstrate the trustworthiness of the DVC analyses.  
271 The RMS residuals wrt. the baseline levels were a bit higher for test B (*i.e.*, 1, 700  
272 gray levels) than for test A (*i.e.*, 1, 475 gray levels).

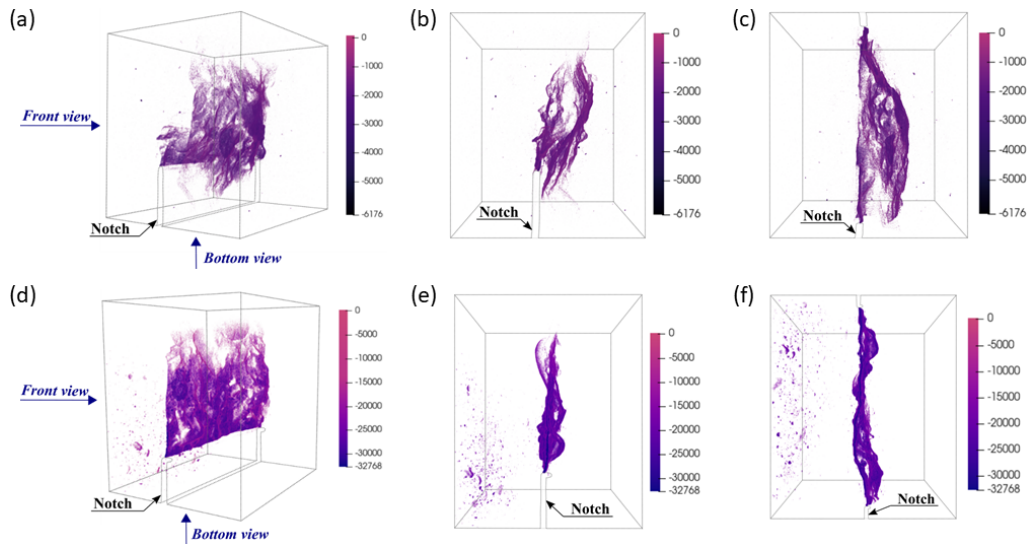


FIGURE 5 – Thresholded gray level residual fields  $\rho$  from DVC analyses ( $l_{reg} = 30$  vx) showing the fractured surfaces. (a-c) Test A, (d-f) test B. (a,d) 3D views, (b,e) front views, and (c,f) bottom views.

273 The deformed meshes and maximum principal strain fields are shown in Fi-  
 274 gure 6 for both tests. The maximum principal strains are localized in the damaged  
 275 zones.

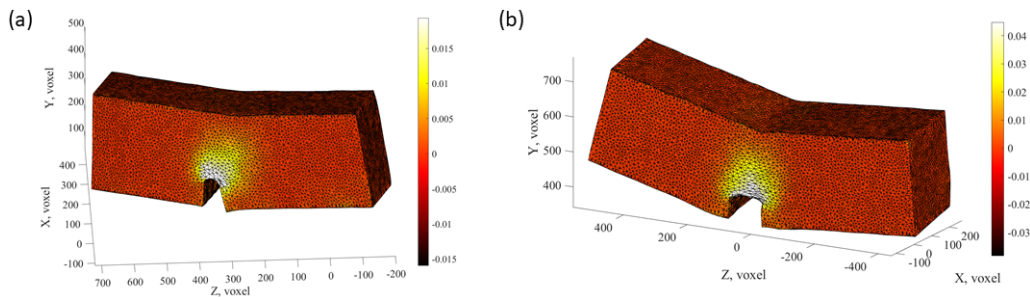


FIGURE 6 – Meshes used in the DVC analyses, deformed according to the measured kinematic fields (amplified  $20\times$ ) displaying maximum principal strain  $\epsilon_1$  fields for tests A (a) and B (b).

276 The kinematic fields measured by DVC with  $l_{reg} = 30$  vx were interpolated  
 277 on the FE meshes. The BCs were determined by interpolating all three displa-  
 278 cement components on three straight lines corresponding to the contact zones  
 279 between the mesobeam and the flexural set-up (Figure 7). The two bottom left

280 and right edges of meshes were defined as the support contact lines and the BCs  
 281 were prescribed directly on these nodes.

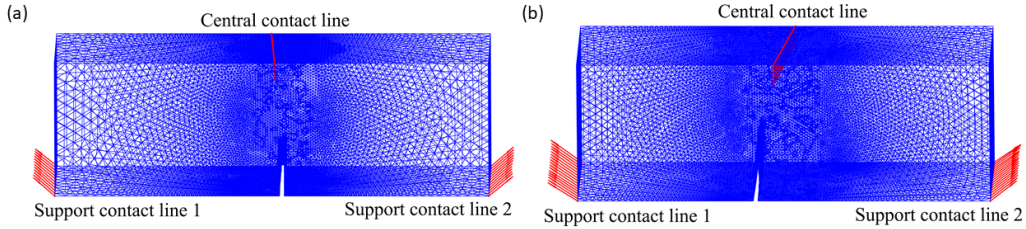


FIGURE 7 – DVC-based boundary conditions for the simulations of tests A (a) and B (b). The displacement vectors are amplified  $40\times$ .

282 Two points at the top front and back edges of the mesh with the maximum ne-  
 283 gative vertical displacement components were defined as the ends of the central  
 284 contact line. This contact line was then discretized with 60 nodes for interpola-  
 285 ting the kinematic boundary conditions. The averages of absolute displacements  
 286 of nodes belonging to different contact zones are reported in Table 4.

TABLE 4 – Average ( $\pm$  standard deviation) displacements of nodes belonging to different contact zones (Figure 7).

BCs	Support contact line 1	Support contact line 2	Central contact line
Test A	$28.0 \pm 0.7 \mu\text{m}$	$30.2 \pm 0.7 \mu\text{m}$	$16.8 \pm 0.3 \mu\text{m}$
Test B	$49.8 \pm 0.4 \mu\text{m}$	$52.9 \pm 0.9 \mu\text{m}$	$31.6 \pm 0.4 \mu\text{m}$

## 287 2.5. Damage modeling

288 In this study, the PFM for brittle materials [45; 46] implemented with an im-  
 289 plicit and staggered scheme was selected to model damage in the bulk cementi-  
 290 tious matrix and limestone aggregates. To study the influence of ITZs on crack  
 291 formation, debonding of matrix-aggregate interfaces was introduced using a mo-  
 292 dified version of the cohesive zone model proposed by Wu et al. [71], which takes  
 293 into account imperfect interfaces [84]. The models are detailed in the following  
 294 sections.

### 295 2.5.1. Phase-field model for a brittle material

296 In PFMs, sharp crack topologies are regularized by introducing a diffuse cra-  
 297 cked zone. The crack surface inside the solid body  $\mathcal{B}$  is described by a functional

298  $\Gamma_l$  dependent upon an auxiliary variable  $d$  (*crack phase field* or damage) and a  
 299 *characteristic length*  $\ell$

$$\Gamma_l(d) = \int_{\mathcal{B}} \gamma_l(d) dV \quad (1)$$

300 with

$$\gamma_l(d) = \frac{d^2}{2\ell} + \frac{\ell}{2} \|\nabla d\|^2 \quad (2)$$

301 where  $\gamma_l$  is the cracked surface density (with  $d = 0$  characterizing the unbroken  
 302 state and  $d = 1$  the fully broken state of the material). The characteristic length  
 303  $\ell$  governs the size of the diffuse cracked zone. When  $\ell$  tends to zero, the material  
 304 response approaches brittle fracture. The consistency of the variational methods  
 305 was proven by  $\Gamma$ -convergence to the Griffith theory as the length scale  $\ell$  tends  
 306 to zero [85].

307 The minimization problem for the cracked surface  $d = \arg\{\inf_{\delta} \Gamma_l(\delta)\}$  in do-  
 308 main  $\mathcal{B}$  gives the crack phase field

$$d(x) = e^{-|x|/\ell} \quad (3)$$

309 The total energy is equal to the sum of the bulk deformation energy  $E_e$  and the  
 310 energy required for crack propagation  $E_d$

$$E_d = \int_{\mathcal{B}} \psi_d dV = \int_{\mathcal{B}} G_f \gamma_l(d) dV \quad (4)$$

311 where  $\psi_d$  is the energy density related to  $E_d$ , and  $G_f$  the fracture energy.

312 Unilateral effects and the degradation of elastic bulk energy in tension are  
 313 taken into account by decomposing the elastic energy into positive and negative  
 314 contributions [45]

$$E_e(d, \epsilon) = \int_{\mathcal{B}} \psi_e dV \quad (5)$$

315 with

$$\psi_e(d, \epsilon) = (g(d) + k)\psi_0^+(\epsilon) + \psi_0^- \quad (6)$$

316 and

$$g(d) = (1 - d)^2 \quad (7)$$

317 where  $\psi_0^+(\epsilon)$  is the extensional energy (*i.e.*, dependent on positive strains),  $\psi_0^-(\epsilon)$   
 318 the contractional energy (*i.e.*, dependent on negative strains),  $g(d)$  the degrada-  
 319 tion function. As  $g(d)$  is specifically associated with the extensional energy, it

320 allows stiffness recovery to be modeled in contraction due to crack closure. The  
 321 small positive parameter  $k \approx 0$  circumvents the full degradation of the energy  
 322 by leaving an “artificial” elastic energy density  $k\psi_0^+(\boldsymbol{\epsilon})$  at fully broken states for  
 323 keeping the problem well-posed.

The extensional and contractional energies read

$$\begin{cases} \psi_0^+(\boldsymbol{\epsilon}) = \frac{\lambda}{2} \{ \langle \text{tr}(\boldsymbol{\epsilon}) \rangle_+ \}^2 + \mu \text{tr} \{ (\boldsymbol{\epsilon}_+)^2 \} & (8) \\ \psi_0^-(\boldsymbol{\epsilon}) = \frac{\lambda}{2} \{ \langle \text{tr}(\boldsymbol{\epsilon}) \rangle_- \}^2 + \mu \text{tr} \{ (\boldsymbol{\epsilon}_-)^2 \} & (9) \end{cases}$$

324 where  $\lambda$  and  $\mu$  are the Lamé coefficients,  $\boldsymbol{\epsilon}$  the elastic strain tensor with spectral  
 325 decomposition into positive  $\boldsymbol{\epsilon}_+$  and negative  $\boldsymbol{\epsilon}_-$  parts

$$\boldsymbol{\epsilon}_+ = \sum_{a=1}^3 \langle \epsilon_a \rangle_+ \mathbf{n}_a \otimes \mathbf{n}_a \quad \boldsymbol{\epsilon}_- = \sum_{a=1}^3 \langle \epsilon_a \rangle_- \mathbf{n}_a \otimes \mathbf{n}_a, \quad \|\mathbf{n}_a\| = 1 \quad (10)$$

326 Here,  $\epsilon_a$  are the elastic tensor eigenvalues and  $\mathbf{n}_a$  the eigen vectors. The operators  
 327  $\langle \blacksquare \rangle_+$  and  $\langle \blacksquare \rangle_-$  are defined as

$$\langle \blacksquare \rangle_+ = \begin{cases} 0, & \blacksquare < 0 & (11) \\ \blacksquare, & \blacksquare \geq 0 & (12) \end{cases} \quad \langle \blacksquare \rangle_- = \begin{cases} \blacksquare, & \blacksquare < 0 & (13) \\ 0, & \blacksquare \geq 0 & (14) \end{cases}$$

329 The variational derivative of the potential energy for irreversible processes  
 330 reads

$$\boldsymbol{\sigma} : \dot{\boldsymbol{\epsilon}} = \dot{\psi} + \phi, \quad \phi \geq 0 \quad (15)$$

331 where  $\boldsymbol{\sigma}$  is the Cauchy stress tensor,  $\dot{\boldsymbol{\epsilon}}$  the strain rate tensor,  $\dot{\psi}$  the Helmholtz free  
 332 power, and  $\phi$  the dissipated power. The stress tensor  $\boldsymbol{\sigma}$  for an isotropic elastic  
 333 medium is written as

$$\boldsymbol{\sigma} = \frac{\partial \psi}{\partial \boldsymbol{\epsilon}} = (\lambda \langle \text{tr} \boldsymbol{\epsilon} \rangle_+ \mathbf{I} + 2\mu \boldsymbol{\epsilon}_+) [(1-d)^2 + k] + \lambda \langle \text{tr} \boldsymbol{\epsilon} \rangle_- \mathbf{I} + 2\mu \boldsymbol{\epsilon}_- \quad (16)$$

334 with  $\mathbf{I}$  the second order identity tensor. Thermodynamic consistency is ensured  
 335 by prescribing a non-negative growth of the crack phase field

$$\dot{d} \geq 0 \quad (17)$$

336 The Helmholtz free power is expressed as

$$\dot{\psi} = \dot{\psi}_d + \dot{\psi}_e = \frac{\partial \psi}{\partial d} \cdot \dot{d} + \frac{\partial \psi}{\partial \boldsymbol{\epsilon}} \cdot \dot{\boldsymbol{\epsilon}} \quad (18)$$

The minimization of Equation (15) with Equation (17) as constraint, yields a thermodynamically consistent phase-field equation for the damage variable  $d$

$$\begin{cases} \left( \frac{G_f}{\ell} + 2\mathcal{H} \right) d - G_f \ell \Delta d = 2\mathcal{H} & \text{in } \mathcal{B} \\ \mathcal{H} = \max_t(\psi^+) \end{cases} \quad (19)$$

337 The temporal changes of the phase field are driven by a local history field  $\mathcal{H}$ ,  
 338 which is equal to the maximum extensional energy obtained in the history of  
 339  $\psi_0^+(\epsilon)$ . The introduction of  $\mathcal{H}$  in the phase-field governing equations allows a  
 340 simplified system of equations to be derived (for more details see [45]).

341 The PFM was implemented in Cast3m and MFront with an implicit and stag-  
 342 gered scheme [63]. In this algorithm, the coupled problem consisting of the  
 343 displacement field  $\mathbf{u}$  and phase-field  $d$  equations is solved by iterative calcula-  
 344 tions. First, a displacement increments  $\Delta \mathbf{u}$  is estimated for the iteration step and  
 345 then mechanical equilibrium is checked. A modified Newton-Raphson scheme  
 346 is used to iteratively update the displacement corrections. Once the latter ones  
 347 are known, other variables (*i.e.*,  $\epsilon$ ,  $\sigma$ ,  $\mathcal{H}$ ) are deduced. They are then used to cal-  
 348 culate  $\Delta d$  from the phase-field equation (19). An iterative fixed-point method is  
 349 followed to achieve convergence on both displacement and phase field equations.  
 350 Convergence is reached when the maximum difference between two successive  
 351 phase fields  $d$  is less than a given threshold.

### 352 2.5.2. Cohesive zone model

353 The cohesive zone model used in this study was proposed by Wu et al. [71],  
 354 and modified to reduce to the so-called Linear Spring Model (LSM) [84; 86; 16]  
 355 for undamaged interfaces. The model was applied to zero-thickness interface  
 356 elements connecting the faces of two adjacent elements. In the case of tetrahedral  
 357 elements, interface elements are triangular surfaces. When the interface is thin  
 358 and compliant with respect to the inclusion, namely,

$$h_{itz} \ll R_{ag}, \quad E_{itz} \ll E_{ag}, \quad \mu_{itz} \ll \mu_{ag} \quad (21)$$

359 where  $E_{itz}$  and  $\mu_{itz}$  are the Young's and shear moduli of the material composing  
 360 the interface, respectively,  $E_{ag}$  and  $\mu_{ag}$  those of the aggregate,  $R_{ag}$  the radius of  
 361 the spherical inclusion, and  $h_{itz}$  the interface thickness, then the elastic proper-  
 362 ties of the interface are estimated with the LSM

$$k_n = \frac{2\mu_{itz}(1 - \nu_{itz})}{h_{itz}(1 - 2\nu_{itz})} \quad (22)$$

363 and

$$k_t = \frac{\mu_{itz}}{h_{itz}} \quad (23)$$

364 where  $k_n$  and  $k_t$  are the interface elastic parameters in the normal and tangential  
 365 directions, respectively, and  $\nu_{itz}$  the Poisson's ratio of the interphase. The ITZs  
 366 in cementitious materials conform partially to the conditions of Equation (21)  
 367 (*i.e.*, the second requirement is not perfectly satisfied).

368 The jump conditions of the traction  $[[\boldsymbol{\sigma}]] \cdot \mathbf{n}$  and displacement vector  $[[\mathbf{u}]]$   
 369 across the interface for the LSM read [86]

$$[[\boldsymbol{\sigma}]] \cdot \mathbf{n} = \mathbf{0}, \quad \mathbf{k} \cdot [[\mathbf{u}]] = \boldsymbol{\sigma} \cdot \mathbf{n} \quad (24)$$

370 where  $\mathbf{n}$  is the normal vector to the interface,  $\mathbf{k}$  the second-order tensor repre-  
 371 senting the interface elastic parameters, and  $[[\cdot]]$  the jump across the interface.

372 To govern interface debonding, an equivalent interface opening displacement  
 373  $\lambda_{itz}$  is introduced to account for the relative displacement between two adjacent  
 374 nodes of a cohesive interface element [71]

$$\lambda_{itz} = \sqrt{\langle u_n \rangle_+^2 + \frac{\sum_{i=1}^2 u_{t,i}^2}{\delta_t}} \quad (25)$$

375 with

$$\delta_t = \frac{k_n}{k_t} \quad (26)$$

where  $u_n$  is the normal displacement jump,  $u_t$  the tangential displacement jump.  
 The nonlinear traction-separation law is formulated as

$$\sigma_c(\lambda_{itz}) = \begin{cases} k_n \lambda_{itz} & \text{if } \lambda_{itz} < \lambda_0 = \frac{f_t^{itz}}{k_n} \\ f_t^{itz} \exp\left(-\frac{f_t^{itz}(\lambda_{itz} - \lambda_0)}{G_f^{itz}}\right) & \text{otherwise} \end{cases} \quad (27)$$

376 where  $\sigma_c$  is the equivalent traction in the interface element,  $\lambda_0$  the yield traction,  
 377  $f_t^{itz}$  the tensile strength of the interface, and  $G_f^{itz}$  the fracture energy of the inter-  
 378 face. The potential  $\Phi$  of the deformed body  $\mathcal{B}$ , in which the debonded interface  
 379 is situated, reads

$$\Phi = \int_{\mathcal{B}} \sigma_c(\lambda_{itz}) dV \quad (29)$$

380 The traction  $\mathbf{t}_c$  has normal  $t_{cn}$  and tangential  $t_{ct,i}$  components

$$\{\mathbf{t}_c\}^\top = \{t_{cn} \quad t_{ct,1} \quad t_{ct,2}\} \quad (30)$$

381 that are formulated as partial derivatives of the potential  $\Phi$  with respect to nor-  
382 mal and tangential displacement jumps

$$t_{cn} = \frac{\partial \Phi}{\partial u_n} = \sigma_c(\lambda_{itz}) \frac{u_n}{\lambda_{itz}} \quad (31)$$

383 and

$$t_{ct,i} = \frac{\partial \Phi}{\partial u_{t,i}} = \sigma_c(\lambda_{itz}) \frac{u_{t,i}}{\delta_t \lambda_{itz}} \quad (32)$$

384 Equations (27)-(28) only apply in mode I opening (*i.e.*,  $u_n > 0$ ). To simulate crack  
385 closure with restoration of the load-bearing capacity in normal direction in com-  
386 pression ( $u_n < 0$ ), the normal traction becomes

$$t_{cn} = k_n u_n \quad (33)$$

### 387 3. Results and Discussion

388 The identification procedure was divided into several steps. First, only the  
389 PFM was used to simulate fracture in the cementitious paste and limestone in-  
390 clusions, whereas ITZs were undamaged. The PFM was initially calibrated ba-  
391 sed on experimental peak forces. Second, imperfect interfaces were added with  
392 the Linear Spring Model (LSM), and the influence of the interphase stiffness on  
393 crack propagation was addressed. Further, a CZM was applied to simulate ITZ  
394 debonding, and its effect was analyzed by comparing the fracture paths with ex-  
395 perimental observations. As mentioned above, the numerical simulations were  
396 carried out using the Cast3m FE code and the MFront generator.

#### 397 3.1. Damage modeling with PFM

398 First, the ITZs were not taken into account and damage was only represen-  
399 ted with the PFM for calibration purposes. The damage model was applied to  
400 the matrix and the limestone aggregates. The characteristic length  $\ell$  has a non-  
401 negligible influence on the material response in the brittle version of the PFM and  
402 is commonly regarded as a material property [87]. The phase-field problem was

403 analytically solved for a homogeneous stress state in a one-dimensional setting,  
 404 deriving the expression for the critical stress  $\sigma_{cr}$  [60]

$$\sigma_{cr} = \frac{9}{16} \sqrt{\frac{EG_f}{6\ell}} \quad (34)$$

405 which is equivalent to the tensile strength  $f_t$ . Thus, the characteristic length  $\ell$  can  
 406 be estimated from the knowledge of the tensile strength  $f_t$ , fracture energy  $G_f$   
 407 and Young's modulus  $E$  of the material. Based on the macroscopic properties of  
 408 the Hardened Cement Paste (HCP), measured on 30-mm samples [88], namely,  
 409  $E = 13.3$  GPa,  $f_t = 2.8$  MPa,  $G_f = 4.7 - 6.6$  N/m, the characteristic length  
 410 deduced from Equation (34) is in the range  $\ell = 0.42 - 0.59$  mm. This estimation  
 411 is less than one order of magnitude lower than the dimensions of the ROIs (*i.e.*, 2.3  
 412 and 1.86 mm) and therefore may lead to very large damaged zones. In microscale  
 413 simulations, it would result in a crack path no longer dependent on the spatial  
 414 distribution of aggregates. Moreover, the tensile strength and fracture energy  
 415 of cementitious materials are dependent on sample dimensions [89]. Since the  
 416 properties of cementitious matrices at the micrometer scale are not precisely  
 417 known, the analytical estimation of  $\ell$  was not possible.

418 Numerical simulations of three-point flexural tests on notched homogeneous  
 419 samples showed that high values of  $\ell$  induced more pronounced pre-peak non-  
 420 linearity in force-CMOD curves and decreased the ultimate load [88]. However,  
 421 the experimental force-CMOD curves could not be acquired in this study. Thus,  
 422 the length  $\ell$  could not be calibrated that way either. Mesoflexural tests on HCP  
 423 showed that the material exhibited a perfectly brittle behavior at micrometer  
 424 scale [90]. Therefore, in this study, the cementitious matrix was assumed to be  
 425 mostly brittle at the mesoscale. In the present version of the PFM, the material  
 426 response becomes brittle as  $\ell \rightarrow 0$  [45]. Further, the parameter must satisfy the  
 427 requirement  $\ell > 2h_{el}$  to obtain mesh-independent results [91; 87]. Therefore, the  
 428 characteristic length  $\ell_m$  was assumed to be small while satisfying the previous  
 429 condition (*i.e.*,  $> 2h_{el} = 64 \mu\text{m}$ ). The characteristic length  $\ell_m$  was set to  $80 \mu\text{m}$   
 430 for the cementitious matrix.

431 The damage parameters of limestone aggregates were assumed to be equal to  
 432 those of the matrix (*i.e.*,  $\ell_{ag,Ca} = \ell_m$ ,  $G_{ag,Ca} = G_{f,m}$ ). The fracture energy  $G_{f,m}$   
 433 of the matrix elements adjacent to homogeneous zones of the beam was set to  
 434 a very high value (*i.e.*, 200 N/m) to prevent non-physical damage that may arise  
 435 due to strain concentrations between heterogeneous and homogeneous regions  
 436 with different mechanical properties. The siliceous aggregates and homogeneous  
 437 zones away from the crack were considered to remain linear elastic. The Young's

438 modulus of the siliceous aggregates was set to  $E_{ag, Si} = 70$  GPa [92], and that  
 439 of limestone inclusions was assumed to be equal to  $E_{ag, Ca} = 50$  GPa [93]. The  
 440 Young's modulus and Poisson's ratio for the cementitious paste were equal to  
 441 experimentally measured values [88].

442 The Young's modulus of the homogeneous zones (Figure 4) was obtained  
 443 by running linear elastic compressive simulations on prismatic heterogeneous  
 444 meshes of ROIs excluding the region with the notch (Figure 8).

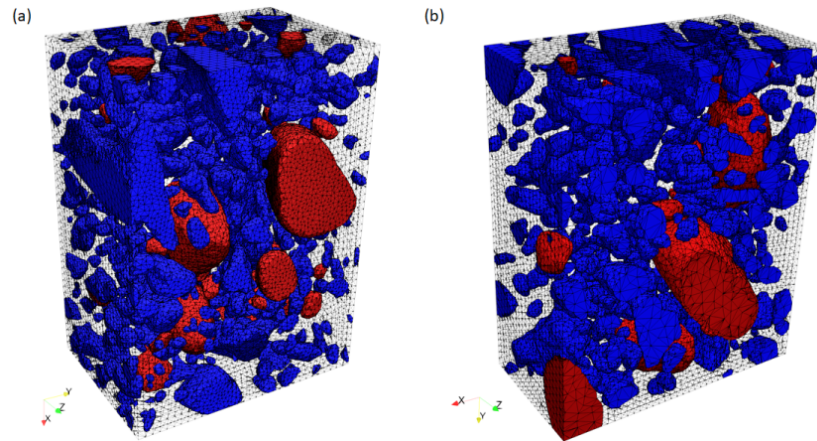


FIGURE 8 – Image-based meshes for the determination of the Young's modulus of mortar for the homogeneous zones (Figure 4) based on (a) ROI A ( $4.54 \times 3.29 \times 2.3$  mm) and (b) ROI B ( $3.65 \times 4.51 \times 1.86$  mm). Blue : siliceous aggregates, red : limestone inclusions, black wireframe : matrix.

445 To estimate upper and lower bounds of the homogenized elastic modulus,  
 446 two types of BCs were used, namely, uniform strain and uniform stress boundary  
 447 conditions, since the first type tends to overestimate the effective properties and  
 448 the latter to underestimate actual levels [94]. The resulting bounds of the effective  
 449 elastic modulus were  $19.7 - 21.3$  GPa for case A, and  $20.0 - 22.1$  GPa for case B.  
 450 The homogenized modulus  $E_{homo}$  was set to 21 GPa, which was approximately  
 451 the average value in both cases. The Poisson's ratio of homogeneous regions was  
 452 set to  $\nu_{homo} = 0.2$ , which corresponds to that of mortar [74]. All the selected  
 453 parameters are gathered in Table 5.

TABLE 5 – Models and parameters for the meshed phases.

Phase	Cementitious matrix	Limestone aggregates	Siliceous aggregates	Homogeneous regions
Constitutive model	Phase Field Model		Linear Elastic Isotropic	
Young's modulus, GPa	$E_m = 13.3$	$E_{ag,Ca} = 50$	$E_{ag,Si} = 70$	$E_{homo} = 21$
Poisson's ratio, -	$\nu_m = 0.25$	$\nu_{ag,Ca} = 0.2$	$\nu_{ag,Si} = 0.2$	$\nu_{homo} = 0.2$
Characteristic length, $\mu\text{m}$	$\ell_m = 80$	$\ell_{ag,Ca} = 80$	-	-

454 The boundary conditions defined in Section 2.4 were interpolated linearly  
 455 over an arbitrary time interval  $t = 0 - 1$ . In test B, crack propagation occurred  
 456 mainly before  $t = 0.5$ . Then, the PFM simulations slowed down and suffered  
 457 from difficult convergence. Therefore, the analyses of test B were terminated at  
 458  $t = 0.5$ . The fracture energy  $G_{f,m}$  was varied in the range  $20 - 35$  N/m in the  
 459 simulations of both tests. The corresponding force-CMOD curves are shown in  
 460 Figure 9. For test A, the best fit was obtained with  $G_{f,m} = 35$  N/m, yet  $G_{f,m} =$   
 461  $30$  N/m also gave very close ultimate forces. In test B, the best approximation  
 462 was obtained when  $G_{f,m} = 25$  N/m. The compromise between both tests was  
 463  $G_{f,m} = 30$  N/m, which gave the closest approximations of both peak forces.

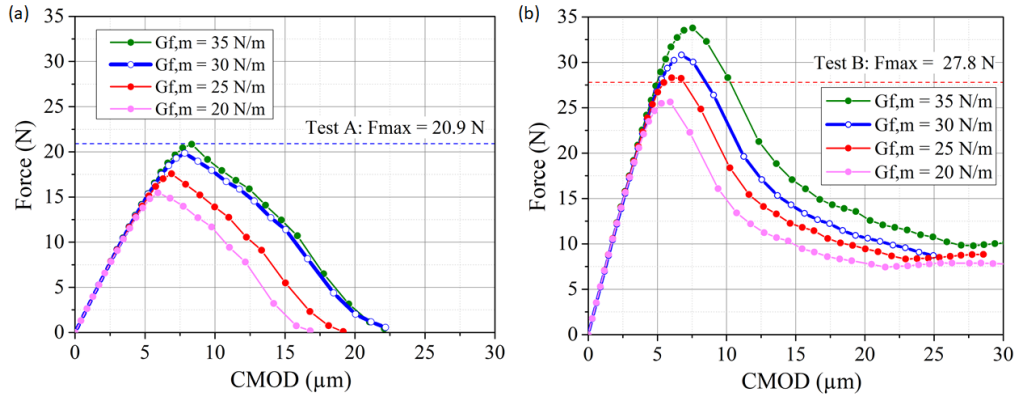


FIGURE 9 – Force-CMOD curves for various  $G_{f,m}$  parameters. (a) Test A, and (b) test B. The variations of peak forces between the two tests could be reproduced thanks to microstructure-based meshes and experimental BCs. The best compromise between both tests was achieved when  $G_{f,m} = 30$  N/m.

464 The simulated crack paths are displayed in Figure 10. It is noted that all frac-  
 465 ture parameters predicted the same crack path in both tests. It is concluded that  
 466 the variation of fracture energy  $G_{f,m}$  did not alter the fracture path when the  
 467 other parameters were kept constant. The variation of the experimental ultimate  
 468 forces was significant (*i.e.*, 27.8 N and 20.9 N). However, these differences could be  
 469 rather well reproduced using the bulk damage model with representative micro-  
 470 structures and boundary conditions. Inaccuracies in flexural strength predictions  
 471 could be due to variations of mechanical properties at lower scales and omitted  
 472 details of the microstructure. However, the agreement between the numerical  
 473 and experimental results is very encouraging given the fact that only one param-  
 474 eter was adjusted.

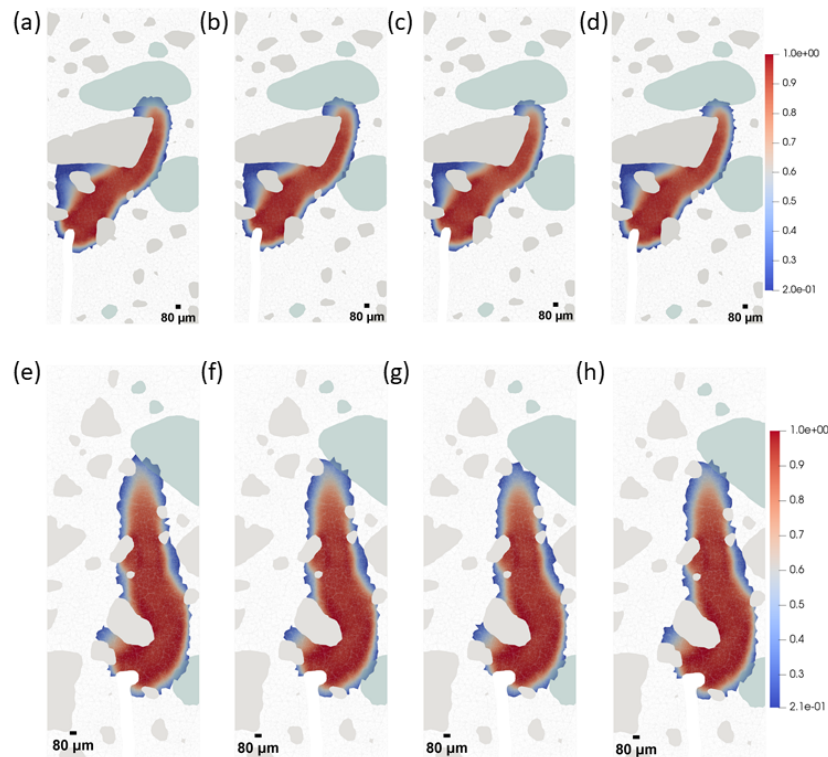


FIGURE 10 – Simulated crack propagation in mesoflexural tests with PFM. Damage fields in the central zones (Figure 4) for test A (a-d) : (a)  $G_{f,m} = 20$  N/m, (b) 25 N/m, (c) 30 N/m, (d) 35 N/m; and test B (e-h) : (e)  $G_{f,m} = 20$  N/m, (f) 25 N/m, (g) 30 N/m, (h) 35 N/m. Cross-sections at  $x = 2.57$  mm depth. Gray wireframe : matrix, gray : siliceous aggregates, light green : limestone aggregates. The variations in  $G_{f,m}$  did not alter the crack patterns.

475 The calibrated fracture energy of the cementitious matrix is much higher  
476 than the level measured in macroscopic tests, namely, 4.7 – 6.6 N/m [88]). In the  
477 PFM for brittle materials, the tensile strength of the material is directly propor-  
478 tional to the fracture energy (Equation (34)). According to statistical size-effects,  
479 a decrease of sample volume leads to a higher strength [95; 96]. Therefore, this  
480 effect may explain the increase in the numerical tensile strength of the cementi-  
481 tious matrix, and consequently, in the fracture energy of PFM in simulations on  
482 small samples. Conversely, the calibrated value of  $G_{f,m}$  is close to levels measu-  
483 red with micro-indentation tests (*i.e.*, 2.51 – 37.82 N/m [97]) and micro-flexural  
484 tests (*i.e.*, 4.4 – 20 N/m [90]). Microscale measurements vary over a wide range  
485 as they correspond to different HCP phases (*e.g.*, calcium silicate hydrate, port-  
486 landite, clinker), while in the numerical simulations the cementitious matrix was  
487 represented as a homogeneous medium. Moreover, the calibrated fracture energy  
488 is valid for the selected characteristic length  $\ell_m$ , since according to Equation (34),  
489 a decrease in  $\ell_m$  for constant  $f_{t,m}$  leads to a decrease in  $G_{f,m}$ .

490 Three-dimensional views of the predicted diffuse crack zones are presented  
491 in Figure 11 at the end of the simulations. The predicted fracture paths are com-  
492 pared with experimental observations in Figures 12 and 13. Since the interface  
493 elements were not considered, the choice of the PFM parameters did not signi-  
494 ficantly influence the crack path. The simulated fracture surfaces followed the  
495 plane passing through the notch root and the loading pin, but their actual path  
496 was affected by the spatial distribution of aggregates.

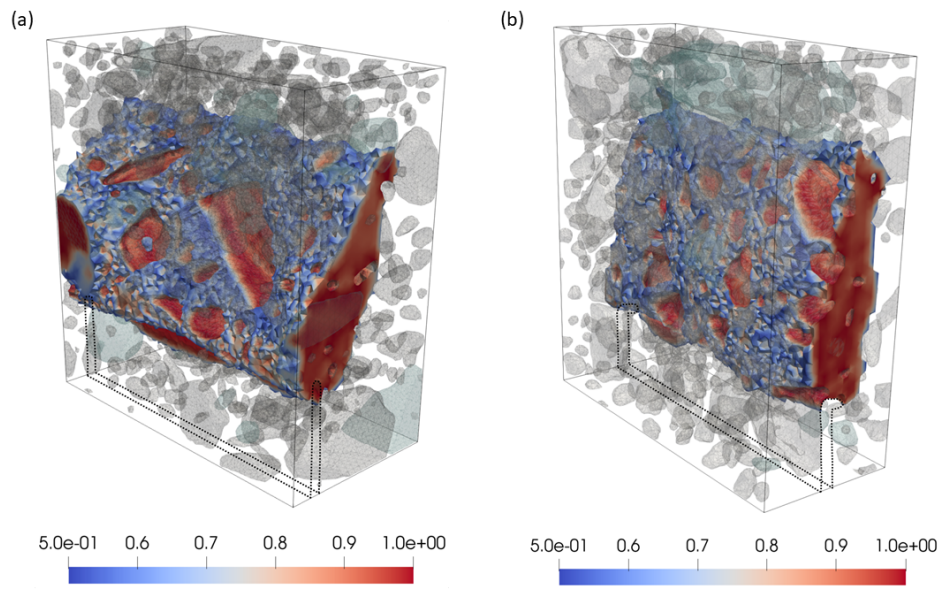


FIGURE 11 – 3D views of thresholded damaged regions of the central zones (Figure 4) predicted by the PFM applied to tests (a) A ( $t = 1.0$ ) and (b) B ( $t = 0.5$ ). Gray : siliceous aggregates, light green : limestone aggregates.

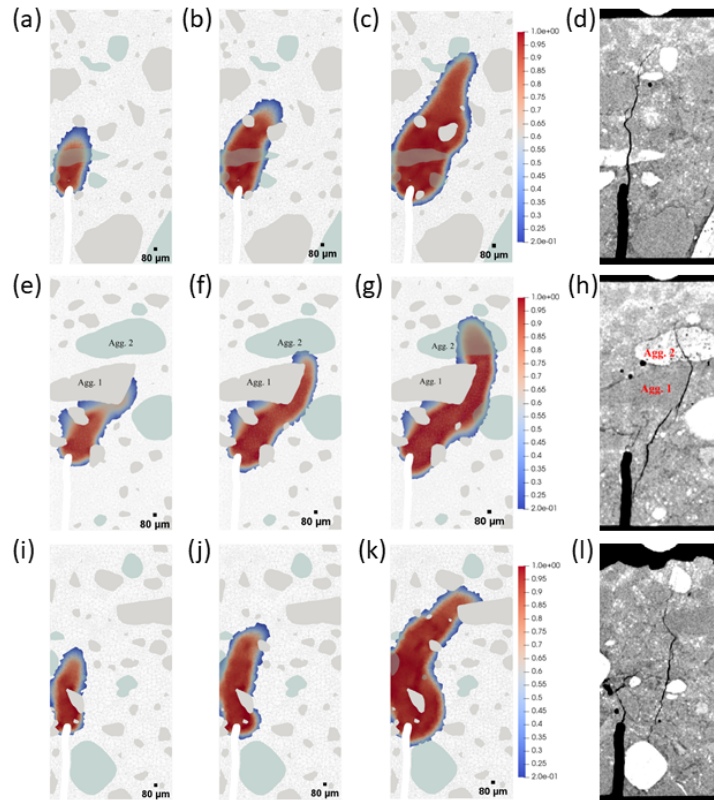


FIGURE 12 – Simulated crack propagation for test A. (a,e,i)  $t = 0.5$ , (b,f,j)  $t = 0.58$ , (c,g,k)  $t = 1.0$ , (d,h,l) XCT sections ( $t = 1.0$ ). Cross-sections at  $x = 0.46$  mm depth (a-d),  $x = 2.57$  mm (e-h),  $x = 4.82$  mm (i-l). The final time step corresponds to  $t = 1.0$ . Gray wireframe : matrix, gray : siliceous aggregates, light green : limestone aggregates. The crack pattern is well reproduced, especially in the middle of the sample, but crack bifurcation was not replicated. The damage zone grew continuously not only vertically but also horizontally.

497 From the damage fields it is observed that, despite the small characteristic  
 498 length, the size of the damage zones could grow to rather large sizes. Moreover,  
 499 the developed damaged zone spanned across the distance between neighboring  
 500 aggregates in the direction perpendicular to the crack propagation path. Thus, it  
 501 is concluded that the fractured zone propagated preferably in matrix regions that  
 502 were not reinforced by inclusions. In a situation where small inclusions are spar-  
 503 sely located in the matrix, the simulated cracked zone may significantly grow in  
 504 size. Moreover, as the fractured zone spread, it continued to increase not only in  
 505 length, but also in width. At later stages, the vertical crack propagation slowed  
 506 down and the damage zone could expand more because of horizontal displace-

507 ments prescribed to the supports. It should be noted that the selected version  
508 of the PFM did not include any threshold for damage initiation, meaning that  
509 damage was induced under any nonzero extensional strain. The absence of an  
510 elastic domain in the current version of the PFM was assumed to be a reason  
511 that leads to thick diffuse damage patterns [87].

512 In experiment A, the fractured surface contained one (Figure 12(d)) or two  
513 (Figure 12(h,l)) cracks depending on the selected cross-section. One of the frac-  
514 tured surfaces started to propagate from the notch root. Figure 12(h) shows a  
515 large aggregate with a vertical interface (Agg.1) that caused a major deviation of  
516 the crack path with subsequent bifurcation. After branching, the fractured sur-  
517 face, which initiated at the notch root, went upward until  $\approx 0.3$  times the ligament  
518 height, while the new branch, located below the loading pin, spanned over the  
519 major part of the specimen height (Figure 12(l)).

520 There was no information about the order in which the fractured branches  
521 were formed. Therefore, it cannot be concluded what was the exact cause of this  
522 phenomenon (*e.g.*, dynamic effects, microstructural details, pre-existing and un-  
523 detected microcracking). This cracking pattern was partially reproduced. The si-  
524 mulated fracture path had only one continuous surface that initiated at the notch  
525 root, and propagated upward. The crack changed its trajectory to bypass the sili-  
526 ceous inclusion Agg.1 (Figure 12(g)), but with no bifurcation. Crack propagation  
527 slowed down when the crack began to cross the limestone particle Agg.2.

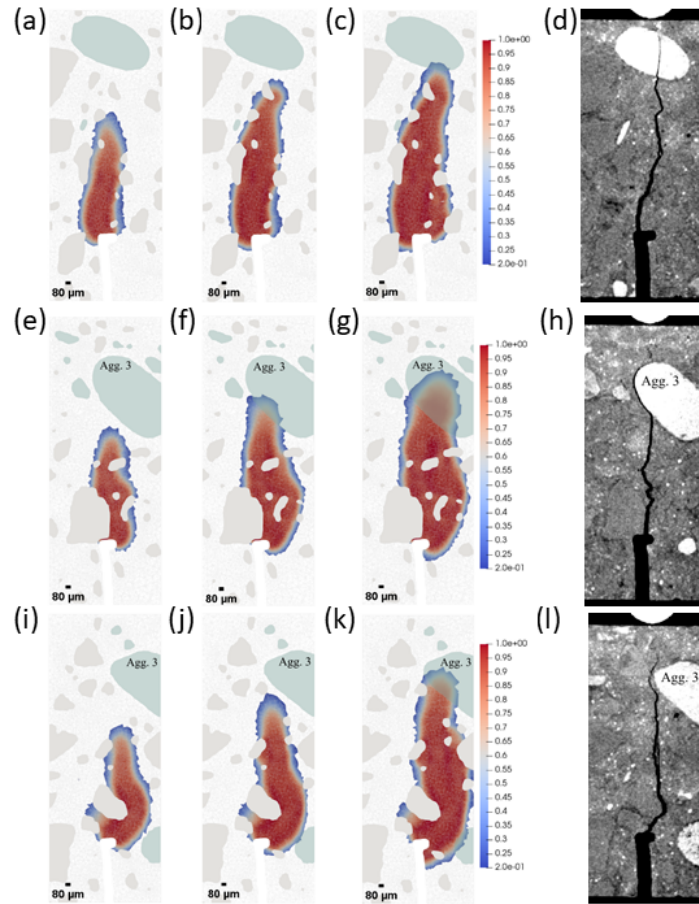


FIGURE 13 – Simulated crack propagation in test B. (a,e,i)  $t = 0.29$ , (b,f,j)  $t = 0.4$ , (c,g,k)  $t = 0.5$ , XCT sections ( $t = 1.0$ ). Cross-sections at  $x = 1.15$  mm depth (a-d),  $x = 2.85$  mm (e-h),  $x = 3.35$  mm (i-l). The final time step corresponds to  $t = 1.0$ . Gray wireframe : matrix, gray : siliceous aggregates, light green : limestone aggregates. The simulated crack path was mostly vertical and flat, which was consistent with experimental observation. At later time steps, the crack grew not only upward but also in width.

528 Test B represented a simpler case since most of the aggregates in the notch-  
 529 load pin plane were relatively small and did not significantly influence the frac-  
 530 ture path. Thus it remained essentially straight and flat. In rare instances, the  
 531 path bypassed larger aggregates (Figure 13(l)). In Figure 13(h), a large limestone  
 532 inclusion (Agg. 3) was not crossed by the crack, unlike in the other cases, but it  
 533 propagated along its interface. Since weaker interface elements were not intro-  
 534 duced in the model and the fracture energies of the matrix and limestone aggre-

535 gates were equal, the diffuse crack propagated inside aggregate 3 (Figure 13(g-k)).  
 536 Overall, the simulated fracture path was consistent with the experiment.

### 537 3.2. Fracture modeling with the PFM and cohesive interfaces

#### 538 3.2.1. Influence of interface stiffness on crack path

539 In a second step, the bulk damage model was enriched with CZMs applied  
 540 to matrix-aggregate interfaces in order to study the influence of stiffness and  
 541 fracture properties of interfaces on crack propagation. Zero-thickness interface  
 542 elements were generated between aggregate and matrix elements in the numeri-  
 543 cal model. The elastic modulus of the interface  $E_{itz}$  was assumed to be equal ap-  
 544 proximately to half of that of cementitious matrix ( $E_{itz} \approx 0.5E_m = 7.0$  GPa) [98].  
 545 The interface Poisson's ratio was assumed to be equal to that of the cementitious  
 546 paste ( $\nu_{itz} = 0.25$ ). The relationship between the tensile strength in the normal  
 547 direction  $f_t^{itz}$  and the maximum traction in the tangential direction  $t_t^{max}$ , based  
 548 on the choice of the interface elastic properties, was  $t_t^{max} = 0.58f_t^{itz}$ . The bulk  
 549 elastic and phase-field parameters were taken constant from Section 3.1. First,  
 550 only the interface stiffness was considered (Table 6). The fracture parameters of  
 551 the CZM (*i.e.*,  $G_f^{itz}$  and  $f_t^{itz}$ ) were set to very high values to prevent any damage  
 552 from occurring in ITZs (*i.e.*, simplifying the CZM model into an LSM model).

TABLE 6 – Initial parameters of the CZM (with no damage).

Parameter	Young's modulus $E_{itz}$ , GPa	Poisson's ratio $\nu_{itz}$ , -	Fracture energy $G_f^{itz}$ , N/m	Tensile strength $f_t^{itz}$ , MPa
Value	7	0.25	$\infty$	$\infty$

553 In Test A, the inclusions had a greater impact on the crack path. Therefore,  
 554 this test was chosen for the initial parametric study of the CZM. In an LSM,  
 555 increasing the thickness  $h_{itz}$  while keeping the Young's modulus  $E_{itz}$  constant  
 556 leads to more compliant interfaces. From a stiffness point of view, this trend is  
 557 interpreted equivalently as inversely varying the Young's modulus at constant  
 558 interface thickness (see Equations (22)-(23)). In the following, the ITZ thickness  
 559  $h_{itz}$  was varied in the range  $0 - 20$   $\mu\text{m}$  [99].

560 The damage fields simulated for different interface thicknesses are presented  
 561 in Figure 14, and the corresponding force-CMOD curves are shown in Figure 15.  
 562 As expected, the damage field for  $h_{itz} \approx 0$   $\mu\text{m}$  was similar to the results in which  
 563 the interfaces were not taken into account (Figure 12). The same remark applies

564 to the corresponding force-CMOD curve. With an increase of the interface thick-  
 565 ness, the crack path changed toward a vertical flat surface. The change of crack  
 566 path influenced the force-CMOD response when  $h_{itz} > 10 \mu\text{m}$  in the post-peak  
 567 part. A flatter segment appeared in the 15 – 20  $\mu\text{m}$  range where fracture propa-  
 568 gation was impeded by an inclusion (Agg. 1). As the crack began to bypass the  
 569 aggregate, the force continued to decrease.

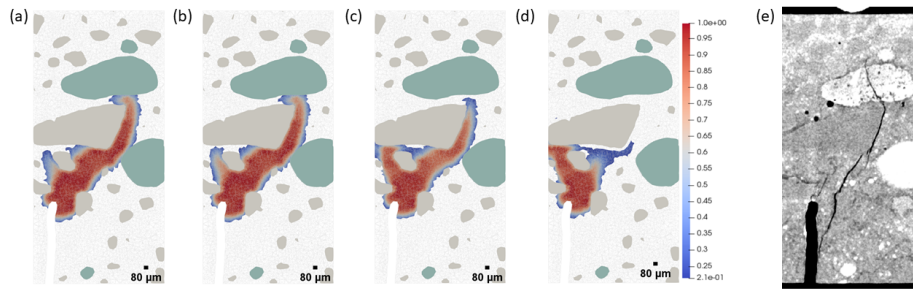


FIGURE 14 – Prediction of crack propagation at  $t = 0.625$ . (a)  $h_{itz} \approx 0 \mu\text{m}$ , (b)  $h_{itz} = 2 \mu\text{m}$ , (c)  $h_{itz} = 10.5 \mu\text{m}$ , (d)  $h_{itz} = 20 \mu\text{m}$ , (e) XCT section at  $t = 1.0$ . Cross-section at  $x = 2.57 \text{ mm}$  depth. Gray wireframe : matrix, gray : siliceous aggregates, light green : limestone aggregates. The final time step corresponds to  $t = 1.0$ . A higher  $h_{itz}$  changed the crack path toward a vertical and flat surface.

570 Compliant and undamageable interfaces modified the crack path as they al-  
 571 lowed for normal displacement and slip between the matrix and inclusions. This  
 572 effect led to stress and strain redistributions in the matrix, which changed the  
 573 crack path. It is concluded that high compliances of the undamageable interfaces  
 574 may lead to a less pronounced dependence of the crack path on the spatial posi-  
 575 tion of the aggregates. In addition, a lower interface stiffness reduced the sample  
 576 global stiffness and flexural strength (Figure 15).

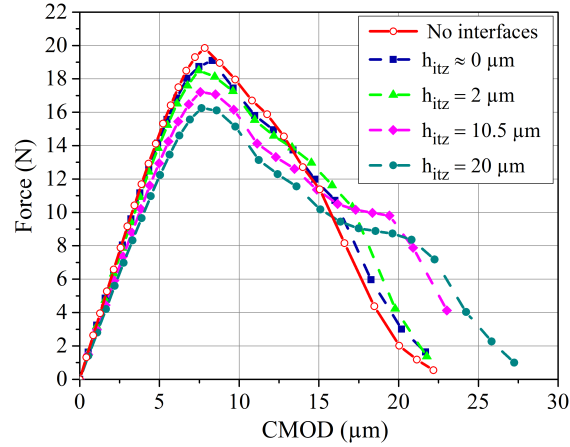


FIGURE 15 – Numerical force-CMOD curves simulated with the PFM ( $G_{f,m} = 30 \text{ N/m}$ ,  $\ell_m = 80 \mu\text{m}$ ) and undamaged cohesive interfaces with different thicknesses. A larger  $h_{itz}$  reduced the sample stiffness and flexural strength.

577 **3.2.2. Influence of interface fracture properties on crack propagation**

578 In the following step, different fracture properties were combined with va-  
 579 rious interface thicknesses. Based on simulation results, two cases were distin-  
 580 guished, namely, compliant interfaces (*i.e.*,  $h_{itz} \geq 2 \mu\text{m}$ ) and rigid interfaces  
 581 (*i.e.*,  $h_{itz} \approx 0 \mu\text{m}$ ).

582 **Compliant interfaces.** The interface thickness was  $h_{itz} = 20 \mu\text{m}$  and  
 583 the fracture energy and tensile strength were varied in the following ranges  
 584  $1 - 20 \text{ N/m}$  and  $1 - 20 \text{ MPa}$ , respectively. The simulated damage fields are  
 585 shown in Figure 16 and the corresponding force-CMOD curves in Figure 17.  
 586 If sufficiently high fracture properties were attributed (*i.e.*,  $f_t^{itz} \geq 20 \text{ MPa}$  and  
 587  $G_f^{itz} \geq 20 \text{ N/m}$ ), the interfaces located far from the crack propagation zone did  
 588 not undergo significant degradation (Figure 16(a)). ITZ debonding occurred only  
 589 in the immediate vicinity of the diffuse damaged zone, which, in turn, facilitated  
 590 crack propagation. In test A, compliant interfaces with high fracture properties  
 591 resulted in a vertical flat fracture surface.

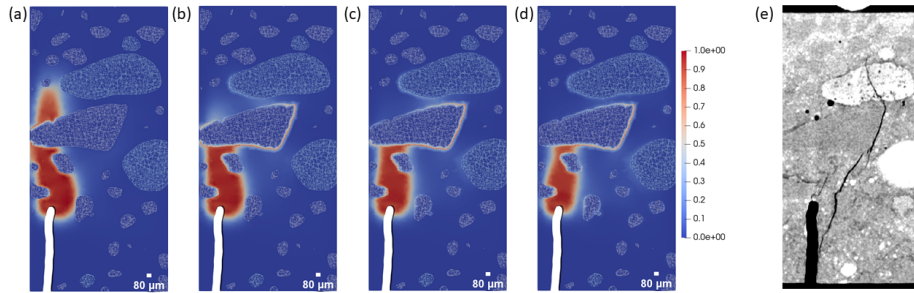


FIGURE 16 – Damage fields with compliant and damageable interfaces ( $h_{itz} = 20 \mu\text{m}$ ). (a)  $f_t^{itz} = 20 \text{ MPa}$ ,  $G_f^{itz} = 20 \text{ N/m}$ . (b)  $f_t^{itz} = 10 \text{ MPa}$ ,  $G_f^{itz} = 10 \text{ N/m}$ . (c)  $f_t^{itz} = 5 \text{ MPa}$ ,  $G_f^{itz} = 5 \text{ N/m}$ . (d)  $f_t^{itz} = 1 \text{ MPa}$ ,  $G_f^{itz} = 1 \text{ N/m}$ . (e) XCT scan. Cross-section at  $x = 2.57 \text{ mm}$  depth. Gray wireframe : siliceous aggregates, light green wireframe : limestone aggregates. High values of  $G_f^{itz}$  and  $f_t^{itz}$  resulted in a vertical and flat crack surface. Low values of  $G_f^{itz}$  and  $f_t^{itz}$  increased the dependence of the crack path on spatial distributions of aggregates.

592 When lower fracture properties were selected (*i.e.*,  $f_t^{itz} < 20 \text{ MPa}$ ,  $G_f^{itz} <$   
 593  $20 \text{ N/m}$ ), interfaces located far from the diffuse damage zone were debonded du-  
 594 ring crack propagation, which modified the strain and stress fields, and caused  
 595 the crack path to deviate. Compliant interfaces with low fracture properties re-  
 596 sulted in fracture paths being more dependent on the internal microstructure.  
 597 The crack path simulated in these cases (Figure 16(b-d)) was closer to that ob-  
 598 served in the experiment compared to the previous case (Figure 16(a)). However,  
 599 it was less accurate than the case when interfaces were not considered at all  
 600 (Figure 12).

601 In the force-CMOD curves (Figure 17), changes in the post-peak region  
 602 are observed compared to undamageable and compliant ITZs. Crack propaga-  
 603 tion was not impeded by aggregates due to interfacial debonding, thus the loss  
 604 of strength was faster. Additionally, low interfacial fracture properties led to  
 605 more pronounced pre-peak nonlinearity. Interface debonding in the area around  
 606 the main crack can be compared to the formation of FPZs that induce quasi-  
 607 brittleness in heterogeneous materials [100]. The choice of fracture parameters  
 608 for ITZs conditions the size of simulated FPZs and, consequently, the quasi-  
 609 brittleness of the sample.

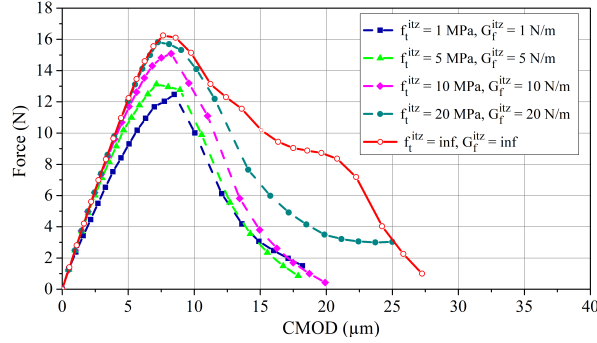


FIGURE 17 – Force-CMOD curves simulated with the PFM ( $G_{f,m} = 30 \text{ N/m}$ ,  $\ell_m = 80 \mu\text{m}$ ) and damageable compliant interfaces ( $h_{itz} = 20 \mu\text{m}$ ) with different fracture properties. Low values of  $G_f^{itz}$  and  $f_t^{itz}$  resulted in more pronounced pre-peak nonlinearity and reduce the flexural strength.

610 Next, simulations with constant and low fracture parameters (*i.e.*,  $f_t^{itz} =$   
 611  $5 \text{ MPa}$  and  $G_f^{itz} = 5 \text{ N/m}$ ) and different interfaces thicknesses ( $h_{itz} = 2$  and  
 612  $20 \mu\text{m}$ ) were performed. In two cases, the same fracture path was reproduced  
 613 (Figure 18(a,b)). The differences in the corresponding force-CMOD histories (Fi-  
 614 gure 18(c)) were only due to different sample rigidity, which depends on the in-  
 615 terface stiffness.

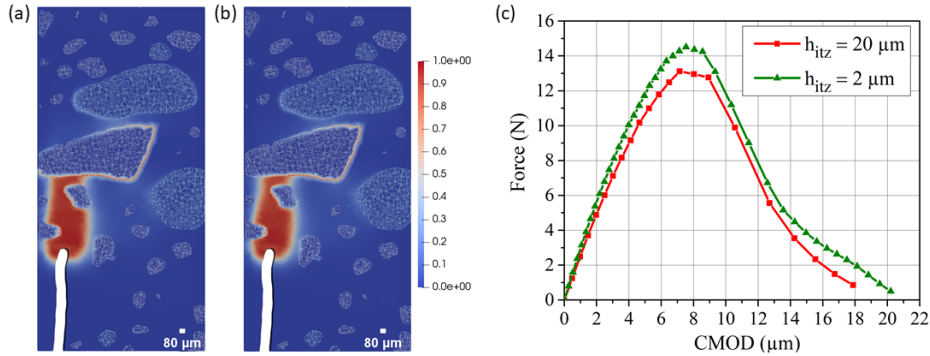


FIGURE 18 – Predicted damage fields with  $f_t^{itz} = 5 \text{ MPa}$ ,  $G_f^{itz} = 5 \text{ N/m}$ . (a)  $h_{itz} = 2 \mu\text{m}$ ,  
 (b)  $h_{itz} = 20 \mu\text{m}$ , (c) corresponding force-CMOD curves. Cross-section at  $x = 2.57 \text{ mm}$  depth.  
 Gray wireframe : siliceous aggregates, light green wireframe : limestone aggregates. Crack  
 patterns in both cases (a-b) were the same. The force-CMOD curves (c) indicated a reduction of  
 the sample rigidity with an increase of  $h_{itz}$ .

616 **Rigid interfaces.** In this subsection, the interface thickness was set to a  
 617 very low value ( $h_{itz} \approx 0 \mu\text{m}$ ). The fracture energy and tensile strength were

618 varied in the ranges of 5 – 30 N/m and 5 – 30 MPa, respectively. In all perfor-  
 619 med runs, the simulations suffered from convergence issues at different stages of  
 620 crack propagation. The damage fields obtained at the last converged time steps  
 621 are reported in Figure 19 (a-b). When lower fracture properties were assigned  
 622 (i.e.,  $f_t^{itz} = 5$  MPa and  $G_f^{itz} = 5$  N/m), divergence in the calculations occur-  
 623 red at earlier stages of crack propagation. In the other cases ( $f_t^{itz} = 30$  MPa,  
 624  $G_f^{itz} = 30$  N/m), the crack could propagate farther, and it was observed that it  
 625 was growing in the vertical direction. A similar fracture path was modeled in the  
 626 previous section with compliant interfaces (Figure 16).

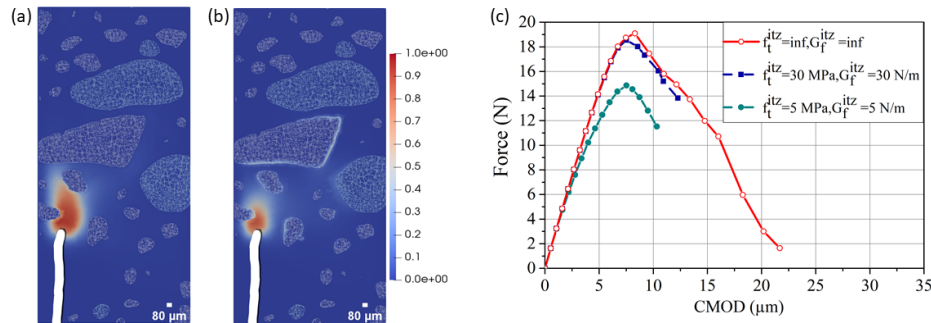


FIGURE 19 – Predicted damage fields with rigid interfaces ( $h_{itz} \approx 0 \mu\text{m}$ ): (a)  $f_t^{itz} = 30$  MPa and  $G_f^{itz} = 30$  N/m, (b)  $f_t^{itz} = 5$  MPa and  $G_f^{itz} = 5$  N/m. Cross-section at  $x = 2.57$  mm depth.

(c) Corresponding force-CMOD curves. The simulations stopped prematurely due to convergence issues. The latest damage fields showed the onset of vertical cracks. Low values of  $G_f^{itz}$  and  $f_t^{itz}$  led to a significant deterioration of the interfaces, resulting in a decrease of flexural strength.

627 The corresponding force-CMOD curves are shown in Figure 19(c). For  $f_t^{itz} =$   
 628 30 MPa,  $G_f^{itz} = 30$  N/m, the force-CMOD curves did not exhibit significant diffe-  
 629 rences in terms of flexural strength and pre-peak nonlinearity in comparison to  
 630 the case with undamageable interfaces. When  $f_t^{itz} = 5$  MPa and  $G_f^{itz} = 5$  N/m,  
 631 a degradation of a large number of interfaces was induced around the main crack,  
 632 thereby resulting in pronounced pre-peak stiffness degradation and re-  
 633 duced strength.

634 ***Influence of interface properties on the propagation of the straight***  
 635 ***crack (test B).*** Simulations with different thicknesses and fracture properties  
 636 for the interfaces were performed for test B for which the damage pattern was  
 637 less dependent on the aggregate distribution (Figures 20-21). When the interfaces  
 638 were undamaged, the simulation with regular interface stiffness ( $h_{itz} = 20 \mu\text{m}$ )

639 reproduced the same crack path as when the CZM was not implemented (Fi-  
 640 gures 20 (a,b)). Interface debonding changed the fracture path (Figures 20(c,d)).  
 641 However, the latter was weakly dependent on the choice of fracture parameters.  
 642 The crack path simulated with the CZM was less accurate than the one modeled  
 643 with bulk damage alone.

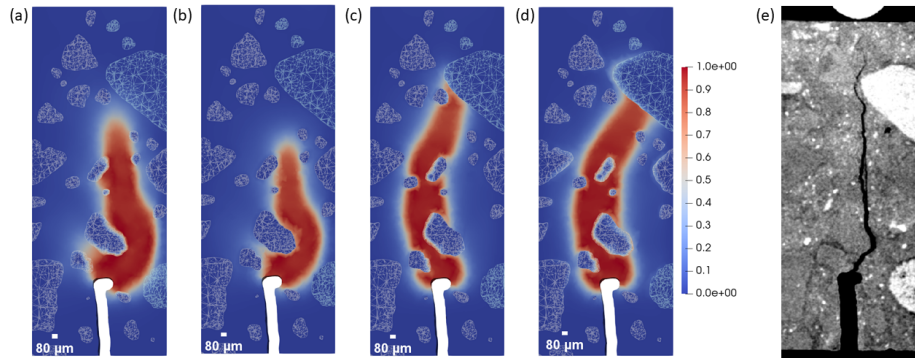


FIGURE 20 – Damage pattern for test B. (a) Perfectly bonded interfaces. (b-d)  $h_{itz} = 20 \mu\text{m}$ .  
 (b)  $f_t^{itz} = \infty$  and  $G_f^{itz} = \infty$ . (c)  $f_t^{itz} = 20 \text{ MPa}$  and  $G_f^{itz} = 20 \text{ N/m}$ . (d)  $f_t^{itz} = 5 \text{ MPa}$  and  
 $G_f^{itz} = 5 \text{ N/m}$ . (e) XCT section at  $x = 2.57 \text{ mm}$  depth. Gray wireframe : siliceous aggregates,  
 light green wireframe : limestone aggregates. The predictions with undamageable and  
 compliant interfaces (b) led to similar results as those obtained with perfectly bonded interfaces  
 (a). Damageable and compliant interfaces with varying fracture properties (c-d) gave a rather  
 different and less consistent crack pattern.

644 Regarding the force-CMOD curves (Figure 21), the simulations of test B sho-  
 645 wed similar effects as observed in test A. The introduction of compliant inter-  
 646 faces reduced the flexural strength and made the pre-peak nonlinearity more  
 647 pronounced. The introduction of ITZ debonding amplified these effects, which  
 648 became more important with decreasing interface fracture properties.

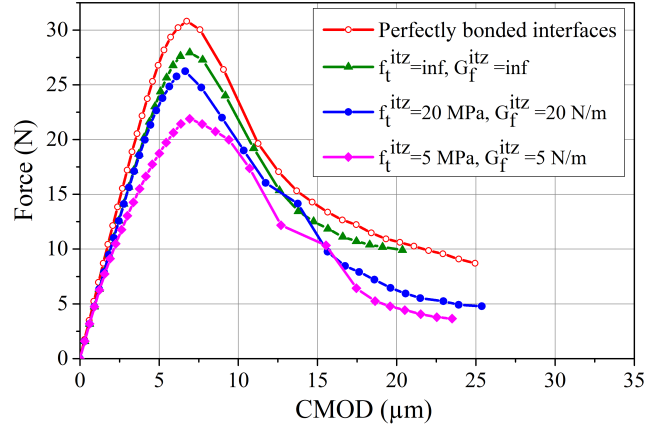


FIGURE 21 – Numerical force-CMOD curves (test B) simulated with the PFM ( $G_{f,m} = 30$  N/m,  $\ell_m = 80$   $\mu\text{m}$ ) and compliant interfaces ( $h_{itz} = 20$   $\mu\text{m}$ ) with different fracture properties. As observed in Figures 15-19, an increase of  $h_{itz}$  reduced the sample stiffness and flexural strength, and increased the pre-peak nonlinearity. Further addition of ITZ debonding made these effects more pronounced.

#### 649 4. Conclusion and Perspectives

650 In this study, several models were tested to represent fracture in cementitious  
 651 bulk matrix (PFM) and at matrix-inclusion interfaces (LSM, CZM) through direct  
 652 simulations of two *in situ* flexural tests on mesoscale samples made of mortar.  
 653 The microscale simulations were based on meshes constructed from CT scans.  
 654 The boundary conditions were obtained by DVC measurements. The fracture  
 655 energy of the matrix was calibrated considering both tests having two different  
 656 types of fractured surfaces (*i.e.*, asymmetric with branching, and symmetric and  
 657 flat). The predicted post-mortem damage patterns were then compared to their  
 658 imaged counter-parts as further validation. The effectiveness of the investigated  
 659 approaches are detailed below.

660 First, the phase field model for brittle materials provided satisfactory results  
 661 in microscopic fracture modeling. The fracture energy of the matrix was effecti-  
 662 vely calibrated to retrieve the experimental peak forces in *both* tests. The simu-  
 663 lated fracture paths were consistent with the experiments thanks to representa-  
 664 tive microstructure and boundary conditions. However, it could not reproduce  
 665 complicated fracture patterns such as bifurcations. The predicted force-CMOD  
 666 curves showed strain hardening before fracture and steady force decrease, cha-  
 667 racteristic of quasi-brittle materials, despite the fact that the cementitious matrix

668 was calibrated for brittle failure. Overall, the selected PFM provided satisfactory  
669 results in microscopic fracture modeling.

670 Second, the introduction of interfacial elements did not significantly improve  
671 the faithfulness of fracture path predictions. Applied to a complex asymmetric  
672 crack path, undamageable interfaces (corresponding to an LSM model) with hi-  
673 gher prescribed thickness, which were more compliant, led to less-dependent  
674 crack paths on the spatial distribution of aggregates, and were less consistent  
675 with the experimental crack path. Conversely, in the case of a flat fractured sur-  
676 face, compliant and imperfect interfaces did not induce significant changes in  
677 the fracture path. In general, the interfaces with smaller thickness gave better  
678 results in terms of predicted crack path.

679 Third, in both tests, the predicted crack path changed when accounting of  
680 ITZ debonding. The asymmetric path depended on the choice of fracture para-  
681 meters. For a flat fracture surface, it was a lot less sensitive to the selected fracture  
682 parameters. It is worth noting that even without the introduction of interface ele-  
683 ments, the diffuse damage zone modeled with the PFM could effectively represent  
684 crack propagation through ITZs. This observation explains the fact that supple-  
685 menting LSM with CZM at matrix-aggregate interfaces could not improve the  
686 crack propagation predictions since it was already well reproduced by the PFM  
687 alone. Regarding the force-CMOD response, the introduction of compliant inter-  
688 faces reduced the flexural strength and made the pre-peak nonlinearity of the  
689 force-CMOD curve more pronounced. ITZ debonding caused further decrease of  
690 flexural strength and pre-peak strain hardening.

691 In further studies, damage models based on the same approach may be ap-  
692 plied for cementitious bulk matrix and matrix-aggregate interfaces for crack  
693 propagation modeling in mortar, as was performed on concrete [37]. The da-  
694 maged region simulated with the PFM tended to be more diffuse perpendicu-  
695 lar to the crack mouth. In future studies, using phase-field models with elastic  
696 domain [101; 102] or phase-field regularized cohesive zone models (PF-CZMs),  
697 which demonstrated lower length scale sensitivity [48; 103], may improve the  
698 localization of damage.

## 699 **5. Acknowledgements**

700 The work reported herein was carried out within the framework of the CEA-  
701 EDF-Framatome agreement.

702 **6. Conflict of interest**

703 The authors declare that they have no conflict of interest.

704 **References**

- 705 [1] Z.-R. Lu, J. Zhou, L. Wang, J. Liu, Damage identification from  
706 static tests by eigenparameter decomposition and sparse regularization,  
707 Structural Health Monitoring 19 (5) (Sep. 2020). doi:10.1177/  
708 1475921719880980.
- 709 [2] H.-L. Minh, S. Khatir, M. Abdel Wahab, T. Cuong-Le, An Enhancing Par-  
710 ticle Swarm Optimization Algorithm (EHVPSO) for damage identifica-  
711 tion in 3D transmission tower, Engineering Structures 242 (2021) 112412.  
712 doi:10.1016/j.engstruct.2021.112412.
- 713 [3] M. Saadatmorad, R.-A. J. Talookolaei, M.-H. Pashaei, S. Khatir, M. A. Wa-  
714 hab, Pearson Correlation and Discrete Wavelet Transform for Crack Ident-  
715 ification in Steel Beams, Mathematics 10 (15) (2022) 2689, number: 15 Pub-  
716 lisher: Multidisciplinary Digital Publishing Institute. doi:10.3390/  
717 math10152689.
- 718 [4] A. Rhardane, F. Grondin, S. Y. Alam, Development of a micro-mechanical  
719 model for the determination of damage properties of cement pastes, Con-  
720 struction and Building Materials 261 (2020) 120514. doi:10.1016/j.  
721 conbuildmat.2020.120514.
- 722 [5] H. Ren, Y. Rong, X. Xu, Mesoscale investigation on failure behavior of  
723 reinforced concrete slab subjected to projectile impact, Engineering Fail-  
724 ure Analysis 127 (2021) 105566. doi:10.1016/j.engfailanal.  
725 2021.105566.
- 726 [6] M. A. Homel, J. Iyer, S. J. Semnani, E. B. Herbold, Mesoscale model and X-  
727 ray computed micro-tomographic imaging of damage progression in ultra-  
728 high-performance concrete, Cement and Concrete Research 157 (2022)  
729 106799. doi:10.1016/j.cemconres.2022.106799.
- 730 [7] X. F. Wang, Z. J. Yang, J. R. Yates, A. P. Jivkov, C. Zhang, Monte Carlo  
731 simulations of mesoscale fracture modelling of concrete with random ag-  
732 gregates and pores, Construction and Building Materials 75 (2015) 35–45.  
733 doi:10.1016/j.conbuildmat.2014.09.069.

- 734 [8] X. Wang, A. P. Jivkov, Combined Numerical-Statistical Analyses of Dam-  
735 age and Failure of 2D and 3D Mesoscale Heterogeneous Concrete, *Mathe-*  
736 *matical Problems in Engineering* 2015 (2015) e702563. doi : 10 . 1155/  
737 2015/702563.
- 738 [9] Q. Xiong, X. Wang, A. P. Jivkov, A 3D multi-phase meso-scale model for  
739 modelling coupling of damage and transport properties in concrete, *Ce-*  
740 *ment and Concrete Composites* 109 (2020) 103545. doi : 10 . 1016/j .  
741 *cemconcomp* . 2020 . 103545.
- 742 [10] D. T. Pham, T. D. Nguyen, M. N. Vu, A. Chinkulkijniwat, Mesoscale ap-  
743 proach to numerical modelling of thermo-mechanical behaviour of con-  
744 crete at high temperature, *European Journal of Environmental and Civil*  
745 *Engineering* 25 (7) (2021) 1329–1348. doi : 10 . 1080/19648189 .  
746 2019 . 1577762.
- 747 [11] P. E. Roelfstra, H. Sadouki, F. H. Wittmann, Le béton numérique, *Matériaux*  
748 *et Constructions* 18 (107) (1985) 327–335.
- 749 [12] J. P. B. Leite, V. Slowik, H. Mihashi, Computer simulation of fracture pro-  
750 cesses of concrete using mesolevel models of lattice structures, *Cement*  
751 *and Concrete Research* 34 (6) (2004) 1025–1033. doi : 10 . 1016/j .  
752 *cemconres* . 2003 . 11 . 011.
- 753 [13] P. Wriggers, S. O. Moftah, Mesoscale models for concrete: Homogenisa-  
754 tion and damage behaviour, *Finite Elements in Analysis and Design* 42 (7)  
755 (2006) 623–636. doi : 10 . 1016/j . *finel* . 2005 . 11 . 008.
- 756 [14] H.-K. Man, J. G. M. van Mier, Influence of particle density on 3D size effects  
757 in the fracture of (numerical) concrete, *Mechanics of Materials* 40 (6) (2008)  
758 470–486. doi : 10 . 1016/j . *mechmat* . 2007 . 11 . 003.
- 759 [15] F. Lavergne, K. Sab, J. Sanahuja, M. Bornert, C. Toulemonde, Investigation  
760 of the effect of aggregates’ morphology on concrete creep properties by  
761 numerical simulations, *Cement and Concrete Research* 71 (2015) 14–28.  
762 doi : 10 . 1016/j . *cemconres* . 2015 . 01 . 003.
- 763 [16] B. Bary, C. Bourcier, T. Helfer, Analytical and 3D numerical analysis of  
764 the thermoviscoelastic behavior of concrete-like materials including in-  
765 terfaces, *Advances in Engineering Software* 112 (2017) 16–30. doi :  
766 10 . 1016/j . *advengsoft* . 2017 . 06 . 006.

- 767 [17] C. E. Torrence, A. Baranikumar, Z. Grasley, W. B. Lawrimore, E. J. Garboczi,  
768 Microstructure homogenization of concrete used in nuclear power plants,  
769 Nuclear Engineering and Design 374 (2021) 111051. doi : 10 . 1016 / j .  
770 nucengdes . 2021 . 111051.
- 771 [18] Z. Yang, X. X. Frank, A heterogeneous cohesive model for quasi-brittle  
772 materials considering spatially varying random fracture properties, Com-  
773 puter Methods in Applied Mechanics and Engineering 197 (45) (2008)  
774 4027–4039. doi : 10 . 1016 / j . cma . 2008 . 03 . 027.
- 775 [19] M. Bruggi, S. Casciati, L. Faravelli, Cohesive crack propagation in a random  
776 elastic medium, Probabilistic Engineering Mechanics 23 (1) (2008) 23–35.  
777 doi : 10 . 1016 / j . probengmech . 2007 . 10 . 001.
- 778 [20] Z. J. Yang, X. T. Su, J. F. Chen, G. H. Liu, Monte Carlo simulation of com-  
779 plex cohesive fracture in random heterogeneous quasi-brittle materials,  
780 International Journal of Solids and Structures 46 (17) (2009) 3222–3234.  
781 doi : 10 . 1016 / j . ijsolstr . 2009 . 04 . 013.
- 782 [21] Y.-j. Huang, H. Zhang, B.-b. Li, Z.-j. Yang, J.-y. Wu, P. J. Withers, Genera-  
783 tion of high-fidelity random fields from micro CT images and phase field-  
784 based mesoscale fracture modelling of concrete, Engineering Fracture  
785 Mechanics 249 (2021) 107762. doi : 10 . 1016 / j . engfracmech .  
786 2021 . 107762.
- 787 [22] E. Maire, P. J. Withers, Quantitative X-ray tomography, International Ma-  
788 terials Reviews 59 (1) (2014) 1–43. doi : 10 . 1179 / 1743280413Y .  
789 0000000023.
- 790 [23] F. Bernachy-Barbe, B. Bary, Effect of aggregate shapes on local fields in  
791 3D mesoscale simulations of the concrete creep behavior, Finite Elements  
792 in Analysis and Design 156 (2019) 13–23. doi : 10 . 1016 / j . finel .  
793 2019 . 01 . 001.
- 794 [24] H.-K. Man, J. G. M. van Mier, Size effect on strength and fracture en-  
795 ergy for numerical concrete with realistic aggregate shapes, Interna-  
796 tional Journal of Fracture 154 (1) (2008) 61–72. doi : 10 . 1007 /  
797 s10704 - 008 - 9270 - y.

- 798 [25] H. K. Man, J. G. M. van Mier, Damage distribution and size effect in numeri-  
799 cal concrete from lattice analyses, *Cement and Concrete Composites* 33 (9)  
800 (2011) 867–880. doi : 10 . 1016 / j . cemconcomp . 2011 . 01 . 008.
- 801 [26] W. Ren, Z. Yang, R. Sharma, C. Zhang, P. J. Withers, Two-dimensional  
802 X-ray CT image based meso-scale fracture modelling of concrete, *En-  
803 gineering Fracture Mechanics* 133 (2015) 24–39. doi : 10 . 1016 / j .  
804 engfracmech . 2014 . 10 . 016.
- 805 [27] W. Ren, Z. Yang, R. Sharma, S. A. McDonald, P. M. Mummery, Three-  
806 Dimensional In Situ XCT Characterisation and FE Modelling of Cracking  
807 in Concrete, *Complexity* 2018 (2018) 3856584. doi : 10 . 1155 / 2018 /  
808 3856584.
- 809 [28] Y. Huang, Z. Yang, W. Ren, G. Liu, C. Zhang, 3D meso-scale fracture  
810 modelling and validation of concrete based on in-situ X-ray Computed  
811 Tomography images using damage plasticity model, *International Jour-  
812 nal of Solids and Structures* 67-68 (2015) 340–352. doi : 10 . 1016 / j .  
813 ijsolstr . 2015 . 05 . 002.
- 814 [29] H. Li, Y. Huang, Z. Yang, K. Yu, Q. M. Li, 3D meso-scale fracture modelling  
815 of concrete with random aggregates using a phase-field regularized cohe-  
816 sive zone model, *International Journal of Solids and Structures* 256 (2022)  
817 111960. doi : 10 . 1016 / j . ijsolstr . 2022 . 111960.
- 818 [30] Y.-j. Huang, Z.-j. Yang, H. Zhang, S. Natarajan, A phase-field cohesive  
819 zone model integrated with cell-based smoothed finite element method  
820 for quasi-brittle fracture simulations of concrete at mesoscale, *Computer  
821 Methods in Applied Mechanics and Engineering* 396 (2022) 115074. doi :  
822 10 . 1016 / j . cma . 2022 . 115074.
- 823 [31] Y.-j. Huang, H. Zhang, J.-j. Zhou, S.-l. Xu, Efficient quasi-brittle fracture  
824 simulations of concrete at mesoscale using micro CT images and a local-  
825 izing gradient damage model, *Computer Methods in Applied Mechanics  
826 and Engineering* 400 (2022) 115559. doi : 10 . 1016 / j . cma . 2022 .  
827 115559.
- 828 [32] M. Zhang, A. P. Jivkov, Microstructure-informed modelling of damage evo-  
829 lution in cement paste, *Construction and Building Materials* 66 (2014) 731–  
830 742. doi : 10 . 1016 / j . conbuildmat . 2014 . 06 . 017.

- 831 [33] J. Y. Buffiere, E. Maire, J. Adrien, J. P. Masse, E. Boller, In Situ Experiments  
832 with X ray Tomography: an Attractive Tool for Experimental Mechan-  
833 ics, *Experimental Mechanics* 50 (3) (2010) 289–305. doi:10.1007/  
834 s11340-010-9333-7.
- 835 [34] Z.-J. Yang, B.-B. Li, J.-Y. Wu, X-ray computed tomography images  
836 based phase-field modeling of mesoscopic failure in concrete, *Engi-  
837 neering Fracture Mechanics* 208 (2019) 151–170. doi:10.1016/j.  
838 engfracmech.2019.01.005.
- 839 [35] R. C. Hurley, D. C. Pagan, An in-situ study of stress evolution and fracture  
840 growth during compression of concrete, *International Journal of Solids  
841 and Structures* 168 (2019) 26–40. doi:10.1016/j.ijsolstr.  
842 2019.03.015.
- 843 [36] W. Trawiński, J. Bobiński, J. Tejchman, Two-dimensional simulations of  
844 concrete fracture at aggregate level with cohesive elements based on X-ray  
845  $\mu$ CT images, *Engineering Fracture Mechanics* 168 (2016) 204–226. doi:  
846 10.1016/j.engfracmech.2016.09.012.
- 847 [37] W. Trawiński, J. Tejchman, J. Bobiński, A three-dimensional meso-scale  
848 modelling of concrete fracture, based on cohesive elements and X-ray  
849  $\mu$ CT images, *Engineering Fracture Mechanics* 189 (2018) 27–50. doi:  
850 10.1016/j.engfracmech.2017.10.003.
- 851 [38] D. Asahina, E. N. Landis, J. E. Bolander, Modeling of phase interfaces dur-  
852 ing pre-critical crack growth in concrete, *Cement and Concrete Compos-  
853 ites* 33 (9) (2011) 966–977. doi:10.1016/j.cemconcomp.2011.  
854 01.007.
- 855 [39] J. Xiao, W. Li, D. J. Corr, S. P. Shah, Effects of interfacial transition zones  
856 on the stress–strain behavior of modeled recycled aggregate concrete,  
857 *Cement and Concrete Research* 52 (2013) 82–99. doi:10.1016/j.  
858 cemconres.2013.05.004.
- 859 [40] O. Stamati, E. Roubin, E. Andò, Y. Malecot, Tensile failure of micro-  
860 concrete: from mechanical tests to FE meso-model with the help of X-  
861 ray tomography, *Meccanica* 54 (4) (2019) 707–722. doi:10.1007/  
862 s11012-018-0917-0.

- 863 [41] Q. Yu, H. Liu, T. Yang, H. Liu, 3D numerical study on fracture process of  
864 concrete with different ITZ properties using X-ray computerized tomog-  
865 raphy, *International Journal of Solids and Structures* 147 (2018) 204–222.  
866 doi : 10 . 1016 / j . i j s o l s t r . 2018 . 05 . 026.
- 867 [42] B. K. Bay, Methods and applications of digital volume correlation, *The*  
868 *Journal of Strain Analysis for Engineering Design* 43 (8) (2008) 745–760.  
869 doi : 10 . 1243 / 03093247JSA436.
- 870 [43] A. Buljac, C. Jailin, A. Mendoza, J. Neggers, T. Taillandier-Thomas,  
871 A. Bouterf, B. Smaniotto, F. Hild, S. Roux, Digital Volume Correlation: Re-  
872 view of Progress and Challenges, *Experimental Mechanics* 58 (5) (2018)  
873 661–708. doi : 10 . 1007 / s11340 - 018 - 0390 - 7.
- 874 [44] R. Vargas, A. Tsitova, F. Bernachy-Barbe, B. Bary, R. B. Canto, F. Hild, On  
875 the identification of cohesive zone model for curved crack in mortar, *Strain*  
876 56 (6) (2020) e12364.
- 877 [45] C. Miehe, M. Hofacker, F. Welschinger, A phase field model for rate-  
878 independent crack propagation: Robust algorithmic implementation based  
879 on operator splits, *Computer Methods in Applied Mechanics and Engi-  
880 neering* 199 (45) (2010) 2765–2778. doi : 10 . 1016 / j . c m a . 2010 .  
881 04 . 011.
- 882 [46] C. Miehe, F. Welschinger, M. Hofacker, Thermodynamically consistent  
883 phase-field models of fracture: Variational principles and multi-field FE  
884 implementations, *International Journal for Numerical Methods in Engi-  
885 neering* 83 (10) (2010) 1273–1311. doi : 10 . 1002 / n m e . 2861.
- 886 [47] V. Verhoosel, R. Borst, A phase-field model for cohesive fracture, *Internat-  
887 ional Journal for Numerical Methods in Engineering* 96 (1) (2013) 43–62.  
888 doi : 10 . 1002 / n m e . 4553.
- 889 [48] J.-Y. Wu, A unified phase-field theory for the mechanics of damage and  
890 quasi-brittle failure, *Journal of the Mechanics and Physics of Solids* 103  
891 (2017) 72–99. doi : 10 . 1016 / j . j m p s . 2017 . 03 . 015.
- 892 [49] Z. H. Khan, M. Amanul Hasan, R. A. Tarefder, Phase field approach to dam-  
893 age and fracture in asphalt concrete using multiscale finite element model-  
894 ing of an instrumented pavement section, *Engineering Fracture Mechan-*

- 895 ics 272 (2022) 108686. doi:10.1016/j.engfracmech.2022.  
896 108686.
- 897 [50] X. Fang, Z. Pan, A. Chen, Phase field modeling of concrete cracking  
898 for non-uniform corrosion of rebar, Theoretical and Applied Fracture  
899 Mechanics 121 (2022) 103517. doi:10.1016/j.tafmec.2022.  
900 103517.
- 901 [51] T. T. Nguyen, J. Yvonnet, Q. Z. Zhu, M. Bornert, C. Chateau, A phase-field  
902 method for computational modeling of interfacial damage interacting with  
903 crack propagation in realistic microstructures obtained by microtomogra-  
904 phy, Computer Methods in Applied Mechanics and Engineering 312 (2016)  
905 567–595. doi:10.1016/j.cma.2015.10.007.
- 906 [52] J. Han, S. Matsubara, S. Moriguchi, K. Terada, Variational crack phase-field  
907 model for ductile fracture with elastic and plastic damage variables, Com-  
908 puter Methods in Applied Mechanics and Engineering 400 (2022) 115577.  
909 doi:10.1016/j.cma.2022.115577.
- 910 [53] T. You, Q.-Z. Zhu, P.-F. Li, J.-F. Shao, Incorporation of tension-compression  
911 asymmetry into plastic damage phase-field modeling of quasi brittle ge-  
912 omaterials, International Journal of Plasticity 124 (2019) 71–95. doi:  
913 10.1016/j.ijplas.2019.08.003.
- 914 [54] S. Liu, Y. Wang, C. Peng, W. Wu, A thermodynamically consistent phase  
915 field model for mixed-mode fracture in rock-like materials, Computer  
916 Methods in Applied Mechanics and Engineering 392 (2022) 114642. doi:  
917 10.1016/j.cma.2022.114642.
- 918 [55] J. Duan, S. Zhou, C. Xia, Y. Xu, A dynamic phase field model for predicting  
919 rock fracture diversity under impact loading, International Journal of Im-  
920 pact Engineering 171 (2023) 104376. doi:10.1016/j.ijimpeng.  
921 2022.104376.
- 922 [56] J. Wei, L. Sun, Interface fracture prediction of multi-material hybrid struc-  
923 tures by modified phase field models, Theoretical and Applied Fracture  
924 Mechanics 121 (2022) 103562. doi:10.1016/j.tafmec.2022.  
925 103562.

- 926 [57] G. A. Francfort, J. J. Marigo, Revisiting brittle fracture as an energy min-  
927 imization problem, *Journal of the Mechanics and Physics of Solids* 46 (8)  
928 (1998) 1319–1342. doi : 10 . 1016/S0022-5096(98)00034-9.
- 929 [58] B. Bourdin, G. A. Francfort, J.-J. Marigo, Numerical experiments in revis-  
930 ited brittle fracture, *Journal of the Mechanics and Physics of Solids* 48 (4)  
931 (2000) 797–826. doi : 10 . 1016/S0022-5096(99)00028-9.
- 932 [59] T. T. Nguyen, J. Yvonnet, Q. Z. Zhu, M. Bornert, C. Chateau, A phase  
933 field method to simulate crack nucleation and propagation in strongly  
934 heterogeneous materials from direct imaging of their microstructure, *En-  
935 gineering Fracture Mechanics* 139 (2015) 18–39. doi : 10 . 1016/j .  
936 engfracmech . 2015 . 03 . 045.
- 937 [60] M. J. Borden, C. V. Verhoosel, M. A. Scott, T. J. R. Hughes, C. M. Landis,  
938 A phase-field description of dynamic brittle fracture, *Computer Methods  
939 in Applied Mechanics and Engineering* 217-220 (2012) 77–95. doi : 10 .  
940 1016/j . cma . 2012 . 01 . 008.
- 941 [61] H. L. Ren, X. Y. Zhuang, C. Anitescu, T. Rabczuk, An explicit phase field  
942 method for brittle dynamic fracture, *Computers & Structures* 217 (2019)  
943 45–56. doi : 10 . 1016/j . compstruc . 2019 . 03 . 005.
- 944 [62] H. Amor, J.-J. Marigo, C. Maurini, Regularized formulation of the vari-  
945 ational brittle fracture with unilateral contact: Numerical experiments,  
946 *Journal of the Mechanics and Physics of Solids* 57 (8) (2009) 1209–1229.  
947 doi : 10 . 1016/j . jmps . 2009 . 04 . 011.
- 948 [63] Y. Lu, T. Helfer, B. Bary, O. Fandeur, An efficient and robust staggered algo-  
949 rithm applied to the quasi-static description of brittle fracture by a phase-  
950 field approach, *Computer Methods in Applied Mechanics and Engineering*  
951 370 (2020) 113218. doi : 10 . 1016/j . cma . 2020 . 113218.
- 952 [64] S. Qiu, Q. Duan, Y. Shao, S. Chen, W. Yao, Adaptive finite element  
953 method for hybrid phase-field modeling of three-dimensional cracks, *En-  
954 gineering Fracture Mechanics* 271 (2022) 108636. doi : 10 . 1016/j .  
955 engfracmech . 2022 . 108636.
- 956 [65] R. Kiran, N. Nguyen-Thanh, K. Zhou, Adaptive isogeometric analy-  
957 sis-based phase-field modeling of brittle electromechanical fracture in

- 958 piezoceramics, *Engineering Fracture Mechanics* 274 (2022) 108738. doi :  
959 10.1016/j.engfracmech.2022.108738.
- 960 [66] K. D. Nguyen, C. E. Augarde, W. M. Coombs, H. Nguyen-Xuan, M. Abdel-  
961 Wahab, Non-conforming multipatches for NURBS-based finite element  
962 analysis of higher-order phase-field models for brittle fracture, *Engi-  
963 neering Fracture Mechanics* 235 (2020) 107133. doi : 10.1016/j.  
964 engfracmech.2020.107133.
- 965 [67] S. Goswami, C. Anitescu, S. Chakraborty, T. Rabczuk, Transfer learning  
966 enhanced physics informed neural network for phase-field modeling of  
967 fracture, *Theoretical and Applied Fracture Mechanics* 106 (2020) 102447.  
968 doi : 10.1016/j.tafmec.2019.102447.
- 969 [68] A. Tsitova, F. Bernachy-Barbe, B. Bary, S. Al Dandachli, C. Bourcier,  
970 B. Smaniotto, F. Hild, Damage Quantification via Digital Volume Corre-  
971 lation with Heterogeneous Mechanical Regularization: Application to an  
972 In Situ Meso-Flexural Test on Mortar, *Experimental Mechanics* (2021).
- 973 [69] T. Wu, A. Carpiuc-Prisacari, M. Poncelet, L. De Lorenzis, Phase-field simu-  
974 lation of interactive mixed-mode fracture tests on cement mortar with full-  
975 field displacement boundary conditions, *Engineering Fracture Mechanics*  
976 182 (2017) 658–688. doi : 10.1016/j.engfracmech.2017.06.  
977 014.
- 978 [70] T. T. Nguyen, J. Yvonnet, M. Bornert, C. Chateau, Initiation and propa-  
979 gation of complex 3D networks of cracks in heterogeneous quasi-brittle  
980 materials: direct comparison between in situ testing-microCT experiments  
981 and phase field simulations, *Journal of the Mechanics and Physics of Solids*  
982 95 (2016) 320. doi : 10.1016/j.jmps.2016.06.004.
- 983 [71] T. Wu, P. Wriggers, Multiscale diffusion–thermal–mechanical cohesive  
984 zone model for concrete, *Computational Mechanics* 55 (5) (2015) 999–1016.  
985 doi : 10.1007/s00466-015-1149-y.
- 986 [72] S. Tandon, K. Faber, Z. Bazant, Crack Stability in the Fracture of Cemen-  
987 titious Materials, *MRS Proceedings* 370 (1994) 387. doi : 10.1557/  
988 PROC-370-387.
- 989 [73] O. Buyukozturk, B. Hearing, Crack propagation in concrete compos-  
990 ites influenced by interface fracture parameters, *International Journal*

- 991 of Solids and Structures 35 (31) (1998) 4055–4066. doi:10.1016/  
992 S0020-7683(97)00300-4.
- 993 [74] R. Vargas, A. Tsitova, F. Bernachy-Barbe, B. Bary, R. B. Canto, F. Hild, On  
994 the identification of cohesive zone model for curved crack in mortar, Strain  
995 (2020).
- 996 [75] C. Bourcier, W. Dridi, L. Chomat, E. Laucoin, B. Bary, E. Adam, Combs:  
997 open source python library for RVE generation. Application to mi-  
998 croscale diffusion simulations in cementitious materials, in: SNA +  
999 MC 2013 - Joint International Conference on Supercomputing in Nu-  
1000 clear Applications + Monte Carlo, EDP Sciences, Paris, France, 2014.  
1001 doi:10.1051/snamc/201402107.  
1002 URL [https://sna-and-mc-2013-proceedings.  
1003 edpsciences.org/articles/snamc/abs/2014/01/  
1004 snamc2013\\_02107/snamc2013\\_02107.html](https://sna-and-mc-2013-proceedings.edpsciences.org/articles/snamc/abs/2014/01/snamc2013_02107/snamc2013_02107.html)
- 1005 [76] S. Roux, F. Hild, P. Viot, D. Bernard, Three dimensional image correla-  
1006 tion from X-Ray computed tomography of solid foam, Comp. Part A 39 (8)  
1007 (2008) 1253–1265.
- 1008 [77] F. Hild, A. Fanget, J. Adrien, E. Maire, S. Roux, Three-dimensional analysis  
1009 of a tensile test on a propellant with digital volume correlation, Archives  
1010 of Mechanics 63 (5-6) (2011) 1–20.
- 1011 [78] F. Hild, S. Roux, D. Bernard, G. Hauss, M. Rebai, On the use of 3D  
1012 images and 3D displacement measurements for the analysis of damage  
1013 mechanisms in concrete-like materials, in: VIII International Conference  
1014 on Fracture Mechanics of Concrete and Concrete Structures FraMCoS-8,  
1015 Toleda, Spain, 2013.  
1016 URL [https://hal.archives-ouvertes.fr/  
1017 hal-01385670](https://hal.archives-ouvertes.fr/hal-01385670)
- 1018 [79] F. Hild, A. Bouterf, S. Roux, Damage Measurements via DIC, Interna-  
1019 tional Journal of Fracture 191 (1-2) (2015) 77–105. doi:10.1007/  
1020 s10704-015-0004-7.
- 1021 [80] H. Leclerc, J. Périé, S. Roux, F. Hild, Voxel-Scale Digital Volume Correla-  
1022 tion, Experimental Mechanics 51 (4) (2011) 479–490. doi:10.1007/  
1023 s11340-010-9407-6.

- 1024 [81] H. Leclerc, J. Périé, F. Hild, S. Roux, Digital volume correlation: What are  
1025 the limits to the spatial resolution?, *Mechanics & Industry* 13 (2012) 361–  
1026 371.
- 1027 [82] T. Taillandier-Thomas, S. Roux, T. F. Morgeneyer, F. Hild, Localized strain  
1028 field measurement on laminography data with mechanical regulariza-  
1029 tion, *Nuclear Instruments and Methods in Physics Research Section B:  
1030 Beam Interactions with Materials and Atoms* 324 (2014) 70–79. doi :  
1031 10 . 1016 / j . nimb . 2013 . 09 . 033.
- 1032 [83] H. Leclerc, J. Neggers, F. Mathieu, F. Hild, S. Roux, Correli 3.0,  
1033 IDDN.FR.001.520008.000.S.P.2015.000.31500, Agence pour la Protection  
1034 des Programmes, Paris (France) (2015).
- 1035 [84] Z. Hashin, Thermoelastic properties of particulate composites with imper-  
1036 fect interface, *Journal of the Mechanics and Physics of Solids* 39 (6) (1991)  
1037 745–762. doi : 10 . 1016 / 0022 - 5096 ( 91 ) 90023 - H.
- 1038 [85] L. Ambrosio, V. M. Tortorelli, Approximation of functional depending on  
1039 jumps by elliptic functional via t-convergence, *Communications on Pure  
1040 and Applied Mathematics* 43 (8) (1990) 999–1036. doi : 10 . 1002 / cpa .  
1041 3160430805.
- 1042 [86] H. L. Duan, X. Yi, Z. P. Huang, J. Wang, A unified scheme for prediction  
1043 of effective moduli of multiphase composites with interface effects. Part I:  
1044 Theoretical framework, *Mechanics of Materials* 39 (1) (2007) 81–93. doi :  
1045 10 . 1016 / j . mechmat . 2006 . 02 . 009.
- 1046 [87] T. K. Mandal, V. P. Nguyen, J.-Y. Wu, Length scale and mesh bias sen-  
1047 sitivity of phase-field models for brittle and cohesive fracture, *Engi-  
1048 neering Fracture Mechanics* 217 (2019) 106532. doi : 10 . 1016 / j .  
1049 engfracmech . 2019 . 106532.
- 1050 [88] A. Tsitova, F. Bernachy, B. Bary, F. Hild, Experimental and numerical  
1051 study of crack propagation with the phase field method: application to  
1052 three-point bending test, in: *Proceedings of 10th International Confer-  
1053 ence on Fracture Mechanics of Concrete and Concrete Structures*, Bay-  
1054 onne, France, 2019, p. 7. doi : 10 . 21012 / FC10 . 233322.
- 1055 [89] A. Carpinteri, G. Ferrara, L. Imperato, Scaling laws for strength and tough-  
1056 ness of disordered materials: A unified theory based on fractal geometry,

- 1057 Engineering Fracture Mechanics 48 (5) (1994) 673–689. doi : 10 . 1016 /  
1058 0013 - 7944 ( 94 ) 90175 - 9.
- 1059 [90] J. Němeček, V. Králík, V. Šmilauer, L. Polívka, A. Jäger, Tensile strength  
1060 of hydrated cement paste phases assessed by micro-bending tests and  
1061 nanoindentation, Cement and Concrete Composites 73 (2016) 164–173.  
1062 doi : 10 . 1016 / j . cemconcomp . 2016 . 07 . 010.
- 1063 [91] T. T. Nguyen, J. Yvonnet, M. Bornert, C. Chateau, K. Sab, R. Romani,  
1064 R. L. Roy, On the choice of parameters in the phase field method  
1065 for simulating crack initiation with experimental validation, Interna-  
1066 tional Journal of Fracture 197 (2) (2016) 213–226. doi : 10 . 1007 /  
1067 s10704 - 016 - 0082 - 1.
- 1068 [92] W. Pabst, E. Gregorová, Elastic properties of silica polymorphs-a review,  
1069 Ceramics - Silikaty 57 (3) (2013) 167–184.
- 1070 [93] A. Mohammed, W. Mahmood, Statistical Variations and New Correlation  
1071 Models to Predict the Mechanical Behavior and Ultimate Shear Strength of  
1072 Gypsum Rock, Open Engineering 8 (1) (2018) 213–226. doi : 10 . 1515 /  
1073 eng - 2018 - 0026.
- 1074 [94] T. Kanit, S. Forest, I. Galliet, V. Mounoury, D. Jeulin, Determination of the  
1075 size of the representative volume element for random composites: statis-  
1076 tical and numerical approach, International Journal of Solids and Struc-  
1077 tures 40 (13) (2003) 3647–3679. doi : 10 . 1016 / S0020 - 7683 ( 03 )  
1078 00143 - 4.
- 1079 [95] W. Weibull, A statistical theory of the strength of materials, Tech. Rep.  
1080 Report 151, Roy. Swed. Inst. Eng. Res. (1939).
- 1081 [96] W. Weibull, A statistical distribution function of wide applicability, ASME  
1082 Journal of Applied Mechanics 18 (3) (1951) 293–297.
- 1083 [97] S. Xu, Y. Feng, J. Liu, Q. Zeng, Micro indentation fracture of cement paste  
1084 assessed by energy-based method: The method improvement and affecting  
1085 factors, Construction and Building Materials 231 (2020) 117136. doi :  
1086 10 . 1016 / j . conbuildmat . 2019 . 117136.
- 1087 [98] Ł. Skarżyński, J. Tejchman, Experimental Investigations of Fracture Pro-  
1088 cess in Concrete by Means of X-ray Micro-computed Tomography, Strain

- 1089 52 (1) (2016) 26–45. doi:[https://doi.org/10.1111/str.](https://doi.org/10.1111/str.12168)  
1090 12168.
- 1091 [99] K. L. Scrivener, A. K. Crumbie, P. Laugesen, The Interfacial Transi-  
1092 tion Zone (ITZ) Between Cement Paste and Aggregate in Concrete, In-  
1093 terface Science 12 (4) (2004) 411–421. doi:10.1023/B:INTS.  
1094 0000042339.92990.4c.
- 1095 [100] R. Zhou, Y. Lu, L.-G. Wang, H.-M. Chen, Mesoscale modelling of size effect  
1096 on the evolution of fracture process zone in concrete, Engineering Fracture  
1097 Mechanics 245 (2021) 107559. doi:10.1016/j.engfracmech.  
1098 2021.107559.
- 1099 [101] L.-M. Schänzel, Phase field modeling of fracture in rubbery and glassy  
1100 polymers at finite thermo-viscoelastic deformations, PhD thesis, Univer-  
1101 sity of Stuttgart, Institute of Applied Mechanics (MIB) (2015). doi:  
1102 <http://dx.doi.org/10.18419/opus-613>.
- 1103 [102] K. Pham, H. Amor, J.-J. Marigo, C. Maurini, Gradient Damage Mod-  
1104 els and Their Use to Approximate Brittle Fracture, International Jour-  
1105 nal of Damage Mechanics 20 (4) (2011) 618–652. doi:10.1177/  
1106 1056789510386852.
- 1107 [103] J.-Y. Wu, V. P. Nguyen, A length scale insensitive phase-field damage model  
1108 for brittle fracture, Journal of the Mechanics and Physics of Solids 119  
1109 (2018) 20–42. doi:10.1016/j.jmps.2018.06.006.